

# The FLAMINGO project: cosmology with the redshift dependence of weak gravitational lensing peaks

Jeger C. Broxterman,<sup>1,2\*</sup> Matthieu Schaller,<sup>1,2</sup> Henk Hoekstra,<sup>2</sup> Joop Schaye,<sup>2</sup> Robert J. McGibbon,<sup>2</sup> Victor J. Forouhar Moreno<sup>2</sup>, Roi Kugel<sup>2</sup> and Willem Elbers<sup>3</sup>

<sup>1</sup>*Lorentz Institute for Theoretical Physics, Leiden University, PO Box 9506, NL-2300 RA Leiden, the Netherlands*

<sup>2</sup>*Leiden Observatory, Leiden University, PO Box 9513, NL-2300 RA Leiden, The Netherlands*

<sup>3</sup>*Institute for Computational Cosmology, Department of Physics, University of Durham, South Road, Durham, DH1 3LE, UK*

arXiv:2412.02736v1 [astro-ph.CO] 3 Dec 2024

Accepted XXX. Received YYY; in original form ZZZ

## ABSTRACT

Weak gravitational lensing (WL) convergence peaks contain valuable cosmological information in the regime of non-linear collapse. Using the FLAMINGO suite of cosmological hydrodynamical simulations, we study the physical origin and redshift distributions of the objects generating WL peaks selected from a WL convergence map mimicking a *Euclid* signal. We match peaks to individual haloes and show that the high signal-to-noise ratio (SNR > 5) WL peaks measured by Stage IV WL surveys primarily trace  $M_{200c} > 10^{14} M_{\odot}$  haloes. We find that the WL peak sample can compete with the purity and completeness of state-of-the-art X-ray and Sunyaev-Zel'dovich cluster abundance inferences. By comparing the distributions predicted by simulation variations that have been calibrated to the observed gas fractions of local clusters and the present-day galaxy stellar mass function, or shifted versions of these, we illustrate that the shape of the redshift distribution of SNR > 5 peaks is insensitive to baryonic physics while it does change with cosmology. The difference highlights the potential of using WL peaks to constrain cosmology. As the number density of WL peaks scales differently with cosmology and baryonic feedback, WL peak statistics can simultaneously calibrate baryonic feedback and constrain cosmology.

**Key words:** gravitational lensing: weak – methods: numerical – large-scale structure of Universe – cosmology: theory

## 1 INTRODUCTION

The cornerstone of modern cosmology is the  $\Lambda$ CDM model, consisting primarily of dark energy ( $\Lambda$ ) and cold dark matter (CDM). The model can predict a wide range of cosmological observables, including the cosmic microwave background (CMB, e.g. [Planck Collaboration et al. 2020a](#)), baryonic acoustic oscillations (BAO, e.g. [DESI Collaboration et al. 2024](#)), and measurements of the luminosity distance ( $D_L$ ) from supernovae (SNe, e.g. [Riess et al. 2021](#)). Other probes, such as redshift-space distortions (RSDs) (e.g. [Scoccimarro 2004](#)), galaxy clustering (e.g. [Cacciato et al. 2009](#)), CMB lensing (e.g. [Planck Collaboration et al. 2020b](#)), and cosmic shear measure the properties of the large-scale structure (LSS) over a range of scales and with cosmic time. Cosmic shear is the distortion of galaxy shapes by weak gravitational lensing (WL) by the large-scale structure, and it is a powerful tool to map the matter distribution in the universe (for a review, see e.g. [Kilbinger 2015](#)). Many of the LSS probes report values of the  $S_8$  parameter that are in mild tension with CMB predictions. This parameter is well constrained by WL inferences and measures a combination of the matter density and the amplitude of density fluctuations. The  $S_8$  tension manifests itself between CMB and cosmic shear (e.g. [Hildebrandt et al. 2017](#); [Asgari et al. 2021](#); [Secco et al. 2022](#); [Dark Energy Survey and Kilo-Degree Survey Collaboration et al. 2023](#)), galaxy clustering (e.g. [Tröster et al. 2020](#);

[Philcox & Ivanov 2022](#)), RSDs (e.g. [Benisty 2021](#)), and thermal Sunyaev-Zel'dovich (tSZ) measurements (e.g. [McCarthy et al. 2014, 2023](#)).

An additional statistic that is used to constrain cosmology is cluster counts (e.g. [Wang & Steinhardt 1998](#); [Reiprich & Böhringer 2002](#); [Manz et al. 2013](#); [Fumagalli et al. 2024](#)). Clusters are the largest virialized structures in the universe, and their number density probes the high-mass end of the halo mass function (HMF), which is sensitive to the amount of matter ( $\Omega_m$ ), its clumpiness ( $\sigma_8$ ), and the evolution of dark energy ( $w_0, w_a$ ) (e.g. [Courtin et al. 2011](#); [Bocquet et al. 2016](#)). For a review, see [Allen et al. \(2011\)](#).

Clusters may be selected through different observables (e.g. optical richness, SZ or X-ray), but selection effects and model assumptions typically limit cluster cosmology inferences (e.g. [Nagai et al. 2007](#); [Kugel et al. 2024b](#)). Whereas a Compton-y selected sample can provide cleaner selection effects, and more accurate mass estimates can be obtained by calibrating mass proxies using lensing measurements, the approach still suffers from not being able to definitively determine the completeness of the sample as clusters may be missing from the sample due to variations in their temperature and gas content (e.g. [Kugel et al. 2024a](#)). Additionally, current cluster inferences require several model assumptions, such as the choice of HMF, the assumed functional form for observable-mass scaling relations and the associated scatter, which may lead to biased results for next-generation measurements that aim to do precision cosmology at the sub-per cent level ([Bocquet et al. 2016](#); [Kugel et al. 2024b](#)).

\* E-mail: broxterman@lorentz.leidenuniv.nl

In this paper, we instead explore a different approach that aims to extract cosmological information by also probing the high-mass end of the HMF as a function of redshift, but that suffers less from selection effects and model assumptions as the selection is carried out using a WL convergence ( $\kappa$ ) map only. By selecting peaks from a WL map, we expect to extract the same (and more) information probed by current cluster analyses, as we will show that the peaks correspond to virtually all the most massive objects in the universe leading to a pure and complete sample. Crucially, the WL selection of these objects is not plagued by the uncertainties originating from assumptions regarding the dynamical state of the galaxy clusters (e.g. relaxedness or hydrostatic equilibrium) nor by scaling relation calibration problems.

This paper focuses on the local maxima in WL convergence maps, commonly referred to as WL peaks (see e.g. Dietrich & Hartlap 2010; Kacprzak et al. 2016; Martinet et al. 2018; Davies et al. 2021, 2022; Li et al. 2023). These peaks are a non-Gaussian statistic and correspond to the most massive objects in the universe that have undergone non-linear collapse and, therefore, contain a wealth of cosmological information (see e.g. Kratochvil et al. 2010). The origin of WL peaks in the context of single, massive objects has been studied using simulations by Hamana et al. (2004), who found that high signal-to-noise ratio (SNR) peaks originate from single massive objects along the line of sight as opposed to several haloes aligned along the line of sight. These results were confirmed by Yang et al. (2011) and Liu & Haiman (2016), who also found that peaks with  $\text{SNR} > 3.5$  can generally be attributed to a single massive halo. The studies broadly agree, but as there are differences in redshift distributions, noise values, methodology, and SNR cuts, the three studies differ in their exact predictions. We aim to further this understanding by considering the analysis in the context of Stage IV WL surveys, i.e. *Euclid* (Euclid Collaboration: Mellier et al. 2024), *Roman* (Spergel et al. 2015), and *Rubin* (LSST Science Collaboration et al. 2009), and by matching individual peaks to haloes to determine the halo mass regimes corresponding to WL peaks of different WL convergence values.

The WL convergence value of a WL peak depends on the lens mass and redshift (as this impacts the WL kernel) and consequently depends on structure formation as more massive structures form at lower redshift, but also on baryonic feedback as this removes mass from the haloes that act as lenses (see e.g. Stanek et al. 2009; Martizzi et al. 2014; Velliscig et al. 2014; Debackere et al. 2022). In Broxterman et al. (2024), we studied how baryonic physics and changes in cosmology impact the counts of WL peaks using the FLAMINGO simulation suite (Schaye et al. 2023; Kugel et al. 2023). There, we showed that the impact of baryonic physics and cosmology on the number density of high-valued WL peaks can be qualitatively understood by considering the impact of feedback processes on the mass of a single halo and the impact of the cosmological parameters (primarily  $\Omega_m$  and  $\sigma_8$ ) on the HMF. Feedback removes gas from the centres of haloes, causing them to be less overdense. Consequently, the WL effect will be smaller, and the peaks they generate will have lower WL convergence values. Hence, there will be fewer (high-valued)  $\kappa$  peaks when haloes experience stronger feedback. Regarding the impact of cosmology,  $\Omega_m$  broadly moves the amplitude of the HMF vertically, and  $\sigma_8$  shifts its exponential cut-off, both causing there to be more/fewer massive haloes in the universe in general, which in turn is also reflected in the number of (high-valued)  $\kappa$  peaks. Whereas the impact of realistic baryonic physics is smaller than currently reasonable changes in cosmology, the two signatures are degenerate, complicating a hypothetical cosmological inference.

In this work, we aim to extend this analysis by including the red-

shift information of the WL peaks. While the number density of WL peaks in  $\kappa$  depends on cosmology and baryonic physics, we expect the formation time of massive objects and corresponding WL peak redshift to depend primarily on cosmology. The formation time of massive haloes should, to first order, not depend on the exact strength of baryonic feedback. Therefore, the redshift distribution of the peaks contains information on when and how much structure in the universe has formed that could be used as an additional probe to constrain cosmology. The redshift dependence of the number density of WL peaks corresponding to these massive objects should be insensitive to baryonic physics. Therefore, we aim to explore the possibility of using the redshift dependence of the number density of WL peaks to constrain cosmology and discriminate between the impact of baryonic feedback and changes in cosmology.

Recently, Harnois-Deraps et al. (2024) carried out an inference using WL peaks selected on tomographic WL convergence maps from the KiDS-1000 and DES Y1 data releases. They found that this can greatly improve the results compared with selecting peaks from a single integrated WL convergence map as it can probe the evolution of the growth of structure, already highlighting the possibility of including redshift information. We aim to assign a redshift to every peak and thus expect to include more redshift information than in their study. Also, Chen et al. (2024) and Chiu et al. (2024) carried out a similar analysis as the idea explored in this paper by using HSC Y3 data and by selecting clusters through the peaks of WL aperture mass maps. Their sample only consists of 149 clusters selected through WL, and they thus cannot yet provide meaningful constraints. Nonetheless, it highlights the viability of the approach. For a recent review of peaks selected from aperture mass maps, see Oguri & Miyazaki (2024).

This paper aims to explore in more detail the origin of WL peaks by linking them to individual haloes and leveraging the baryonic insensitivity of their redshift distribution to illustrate their potential to better constrain cosmological parameters. To this end, we use the baryonic physics and cosmology variations of the cosmological hydrodynamical simulation suite FLAMINGO (Schaye et al. 2023; Kugel et al. 2023). We first briefly summarize the relevant WL theory in Section 2. We generate full-sky WL convergence maps mimicking the signal of Stage IV WL surveys, as described in Section 3, where we also introduce the algorithm to match individual peaks to massive haloes each. The results of the halo-peak matching and the evolution of the redshift number density of WL peaks are presented in Section 4. The main conclusions are summarized in Section 5.

## 2 THEORY

As we will construct full-sky WL maps from discretized mass shells spaced linearly in redshift, we first summarize the main equations relevant to WL. For full reviews of the WL formalism, see Bartelmann & Schneider (2001); Hoekstra & Jain (2008); Kilbinger (2015). In WL, where the light deflections are small, the magnification matrix ( $A$ ), which describes the linear transformation from the observed angular position ( $\theta$ ) to the unlensed position, is typically decomposed as

$$A_{ij} = \frac{\partial(\delta\theta_i)}{\partial\theta_j} \approx \begin{pmatrix} 1 - \kappa - \gamma_1 & -\gamma_2 \\ -\gamma_2 & 1 - \kappa + \gamma_1 \end{pmatrix}, \quad (1)$$

where  $\kappa$  is the WL convergence and  $\gamma = \gamma_1 + i\gamma_2$  is the WL shear. When assuming the deflections are small, the deflection angle can be expressed as the gradient of the potential ( $\Phi$ ) that is the solution of the 2D Poisson equation,  $\nabla^2\Phi = 4\pi G a^2 \bar{\rho} \delta$ , where  $G$  is the gravitational

constant,  $a$  the scale factor,  $\bar{\rho}$  the mean density of the universe, and  $\delta$  the matter overdensity. By assuming the Born approximation, i.e. evaluating the lensing equations on unperturbed photon paths, the magnification matrix reduces to

$$A_{ij} = \delta_{ij} - \partial_i \partial_j \psi, \quad (2)$$

with  $\psi$  the lensing potential,

$$\psi(\theta, \chi) = \frac{2}{c^2} \int_0^\chi d\chi' \frac{\chi - \chi'}{\chi \chi'} \Phi(\chi' \theta, \chi'), \quad (3)$$

where  $c$  is the speed of light, and we assumed a flat universe such that the comoving angular diameter distance,  $f_K(\chi)$ , reduces to the comoving distance,  $\chi$ . By substituting the Poisson equation, the WL convergence can be estimated as

$$\kappa(\theta, \chi) = \frac{3\Omega_m H_0^2}{2c^2} \int_0^{\chi_{\text{hor}}} d\chi [1 + z(\chi)] W(\chi) \delta(\chi, \theta), \quad (4)$$

where  $H_0$  is the Hubble constant,  $\Omega_m \equiv \rho_m/\rho_{\text{crit},0}$  is the matter density parameter,  $\rho_{\text{crit},0} = 3H_0^2/(8\pi G)$  is the present-day critical density of the universe, and  $z$  is the redshift.  $\chi_{\text{hor}}$  is the comoving line of sight horizon to the edge of the galaxy sample. The weak lensing kernel  $W$  is given by (Kaiser 1992)

$$W(\chi) = \chi \int_\chi^{\chi_{\text{hor}}} d\chi' n_s(\chi') \frac{\chi' - \chi}{\chi'}, \quad (5)$$

where  $n_s(\chi)$  is the comoving source distribution which is normalised ( $\int n_s(\chi) d\chi = 1$ ) and is related to the source redshift distribution as  $n_s(z) dz = n_s(\chi) d\chi$ .

Lu & Haiman (2021) have argued that for a Stage III WL peak inference assuming the Born approximation leads to biased results, and a more sophisticated approach such as backward ray tracing should be applied. In this paper, we do not aim to carry out parameter inference but are instead interested in the origin and redshift evolution of a sample of high-valued WL peaks. Although the exact number of WL peaks at fixed WL convergence values may differ slightly depending on the map construction algorithm, we do not expect the origin of these peaks to change, as they should still stem from the same massive structures in the universe. As the Born approximation facilitates a more straightforward and computationally less expensive way to assign a redshift (as will become clear in Section 3.2), we adopt it in our analysis. Additionally, as we ignore several second-order effects such as lens-lens coupling (Bernardeau et al. 1997), and possible biasing factors such as dilution by cluster member contamination (Applegate et al. 2014; Medezinski et al. 2018) and source clustering (Gatti et al. 2023), the analysis is to some extent idealized.

### 3 METHODS

#### 3.1 FLAMINGO

We use the recently developed FLAMINGO cosmological hydrodynamical simulation suite for our analysis. In this section, we only provide a brief summary of the simulation characteristics; for a detailed description of the simulations and calibration, see Schaye et al. (2023) and Kugel et al. (2023). The simulations were run using the SPHENIX smoothed particle hydrodynamics implementation (Borrow et al. 2022) in SWIFT (Schaller et al. 2024). The simulations include an element-by-element based radiative cooling and heating (Ploeckinger & Schaye 2020), star formation (Schaye & Dalla Vecchia 2008), time-dependent stellar mass loss (Wiersma et al. 2009), and massive neutrinos (Elbers et al. 2021). Supernova and stellar

feedback is kinetic and conserves energy and linear and angular momentum (Dalla Vecchia & Schaye 2008; Chaikin et al. 2023). The AGN feedback is either thermal (Booth & Schaye 2009) or kinetic jet-like, where particles are kicked along the black hole (BH) spin axis (Huško et al. 2022). The simulations are calibrated using machine learning to the galaxy stellar mass function at  $z = 0$  and the gas fraction of low- $z$  clusters and groups of clusters, or systematic shifts in these observables, while taking into account observational uncertainties and biases (Kugel et al. 2023).

In Table 1, we list the simulation parameters directly relevant to the interpretation of our results. The first column lists the simulation's identifier, which is set by the box size in comoving Gpc (cGpc) and  $\log_{10}$  baryonic particle mass. For example, the flagship simulation, L2p8\_m9, has  $5040^3$  baryonic and dark matter (DM) particles and  $2800^3$  massive neutrino particles in a 2.8 cGpc box and an initial mean gas particle mass of  $1.07 \times 10^9 M_\odot$ . All 7 cosmology and 8 baryonic feedback variations were carried out in 1 cGpc boxes with an equal number of particles. The fiducial model in this box is L1\_m9. L1\_m8 and L1\_m10 are variations with the same cosmology and calibrated to the same observational data but with 8 times more and fewer particles, respectively. We will use these to quantify the numerical convergence with resolution. All cosmology variations have an accompanying CDM + neutrino run identified by the post-fix \_DMO.

The eight variations with different baryonic feedback prescriptions were each calibrated to a (shifted) set of observables, as indicated by the fourth and fifth columns in Table 1. These variations vary the cluster gas fractions ( $\Delta f_{\text{gas}}$ ) and/or the galaxy stellar mass function ( $\Delta M_*$ ) by a set amount of observational standard deviations ( $\sigma$ ). The baryonic variations are identified by their shifts in observables, as indicated in the first column of Table 1.

All baryonic variations assume the DES Y3 '3  $\times$  2pt + All Ext.' best-fitting  $\Lambda$ CDM cosmology from Abbott et al. (2022), see also Table 1. Additional cosmology variations were run using the Planck Collaboration et al. (2020a) best-fitting  $\Lambda$ CDM model assuming  $\sum m_\nu c^2 = 0.06$  eV ('Planck'), and variations with heavier neutrinos,  $\sum m_\nu c^2 = 0.24$  eV ('PlanckNu0p24Var', 'PlanckNu0p24Fix') and  $\sum m_\nu c^2 = 0.48$  eV ('PlanckNu0p48Fix'). The PlanckNu0p24Var and PlanckNu0p24Fix differ in their treatment of the other cosmological parameters while changing the neutrino mass. We include two variations with decaying cold dark matter (DCDM) from Elbers et al. (2024). In these simulations, dark matter decays to dark radiation as specified by the decay rate  $\Gamma$  in units  $H_0/h$ , as indicated by the final column in Table 1. Finally, we use a simulation with a 'lensing cosmology' with a lower value of  $\sigma_8$  ('LS8') from Amon et al. (2023) that is consistent with BOSS DR12 galaxy clustering (Reid et al. 2016), and galaxy-galaxy lensing from KiDS-1000 (Asgari et al. 2021), DES Y3 (Abbott et al. 2022), and HSC Y1 (Aihara et al. 2018).

#### 3.1.1 Mass maps

We use the FLAMINGO mass maps to construct our WL convergence maps. These are a set of concentric spherical HEALPix (Górski et al. 2005) surfaces on which the particles that contribute to an observer's past light-cone are projected (see Appendix A2 of Schaye et al. 2023). The L1 and L2p8 simulations have 2 and 8 virtual observers, respectively. The light-cone consists of 60 shells of equal thickness (in redshift) between  $z = 0$  and 3 ( $\Delta z = 0.05$ ). These maps are the input for constructing the WL convergence maps. To allow the use of all functionality of HEALPY (Zonca et al. 2019), we downsample the FLAMINGO maps to  $N_{\text{side}} = 8192$ , corresponding to an angular

**Table 1.** Simulation variations. From left to right, the columns list the simulation identifier; the box size,  $L$ ; the number of baryonic and dark matter particles,  $N_p$ ; the initial mean baryonic particle mass,  $m_b$ ; the shift in the number of standard deviations ( $\sigma$ ) applied to the observational data used in the calibration for the  $z = 0$  galaxy stellar mass function ( $\Delta M_*$ ) and the gas fraction of low-redshift clusters ( $\Delta f_{\text{gas}}$ ); the mode of AGN feedback; the dimensionless Hubble constant,  $h$ ; the present-day total matter density parameter,  $\Omega_m$ ; the present-day baryonic matter density parameter,  $\Omega_b$ ; the sum of neutrino species particle masses,  $\sum m_\nu c^2$ ; the amplitude of the initial power spectrum parametrized as the rms mass density fluctuation in spheres with radius 8 Mpc/h extrapolated to  $z = 0$  using linear theory,  $\sigma_8$  and, if applicable, the dark matter decay rate,  $\Gamma$ .

Identifier	$L$ cGpc	$N_p$	$m_b$ $\times 10^9 M_\odot$	$\Delta M_*$ $\sigma$	$\Delta f_{\text{gas}}$ $\sigma$	AGN	$h$	$\Omega_m$	$\Omega_b$	$\sum m_\nu c^2$ eV	$\sigma_8$	$\Gamma$ $H_0/h$
L2p8_m9	2.8	5040 <sup>3</sup>	1.07	0	0	thermal	0.681	0.306	0.0486	0.06	0.807	–
L1_m9	1	1800 <sup>3</sup>	1.07	0	0	thermal	0.681	0.306	0.0486	0.06	0.807	–
L1_m8	1	3600 <sup>3</sup>	0.134	0	0	thermal	0.681	0.306	0.0486	0.06	0.807	–
L1_m10	1	900 <sup>3</sup>	8.56	0	0	thermal	0.681	0.306	0.0486	0.06	0.807	–
fgas+2 $\sigma$	1	1800 <sup>3</sup>	1.07	0	+2	thermal	0.681	0.306	0.0486	0.06	0.807	–
fgas-2 $\sigma$	1	1800 <sup>3</sup>	1.07	0	-2	thermal	0.681	0.306	0.0486	0.06	0.807	–
fgas-4 $\sigma$	1	1800 <sup>3</sup>	1.07	0	-4	thermal	0.681	0.306	0.0486	0.06	0.807	–
fgas-8 $\sigma$	1	1800 <sup>3</sup>	1.07	0	-8	thermal	0.681	0.306	0.0486	0.06	0.807	–
$M^*-\sigma$	1	1800 <sup>3</sup>	1.07	-1	0	thermal	0.681	0.306	0.0486	0.06	0.807	–
$M^*-\sigma$ _fgas-4 $\sigma$	1	1800 <sup>3</sup>	1.07	-1	-4	thermal	0.681	0.306	0.0486	0.06	0.807	–
Jet	1	1800 <sup>3</sup>	1.07	0	0	jet	0.681	0.306	0.0486	0.06	0.807	–
Jet_fgas-4 $\sigma$	1	1800 <sup>3</sup>	1.07	0	-4	jet	0.681	0.306	0.0486	0.06	0.807	–
Planck	1	1800 <sup>3</sup>	1.07	0	0	thermal	0.673	0.316	0.0494	0.06	0.812	–
PlanckNu0p24Var	1	1800 <sup>3</sup>	1.06	0	0	thermal	0.662	0.328	0.0510	0.24	0.772	–
PlanckNu0p24Fix	1	1800 <sup>3</sup>	1.07	0	0	thermal	0.673	0.316	0.0494	0.24	0.769	–
PlanckNu0p48Fix	1	1800 <sup>3</sup>	1.07	0	0	thermal	0.673	0.316	0.0494	0.48	0.709	–
PlanckLCDM12	1	1800 <sup>3</sup>	1.07	0	0	thermal	0.673	0.274	0.0494	0.06	0.794	0.12
PlanckLCDM24	1	1800 <sup>3</sup>	1.07	0	0	thermal	0.673	0.239	0.0494	0.06	0.777	0.24
LS8	1	1800 <sup>3</sup>	1.07	0	0	thermal	0.682	0.305	0.0473	0.06	0.760	–

resolution of  $\approx 25.8$  arcsec. We then transform the total matter shells at each shell  $i$  into overdensity shells,  $\delta_i(\theta)$ , using

$$\delta_i(\theta) = \frac{\Sigma_i(\theta) - \bar{\Sigma}_i}{\bar{\Sigma}_i}, \quad (6)$$

where  $\Sigma_i(\theta)$  is the surface matter density at shell  $i$  at position  $\theta$  and  $\bar{\Sigma}_i$  is the mean surface matter density, which we evaluate directly from the shell. Because of the discrete redshifts of the FLAMINGO mass maps, we transform the analytic expressions to estimate the WL convergence (equations 4 & 5) to discrete sums given by (e.g. McCarthy et al. 2018)

$$\kappa(\theta) = \frac{3\Omega_m H_0^2}{2c^2} \sum_{i=1}^N [1 + z(\chi_i)] W(\chi_i) \delta_i(\theta) \Delta\chi_i, \quad (7)$$

and

$$W(\chi_i) = \chi_i \sum_{j=i}^N \Delta\chi_j n_s(\chi_j) \frac{\chi_j - \chi}{\chi_j}, \quad (8)$$

respectively. In our analysis, we assume a *Euclid*-like source redshift distribution given by (Euclid Collaboration: Blanchard et al. 2020):

$$n_s(z) \propto \left(\frac{z}{z_0}\right)^2 \exp\left[-\left(\frac{z}{z_0}\right)^{3/2}\right], \quad (9)$$

with  $z_0 = 0.9/\sqrt{2}$ .

We randomly rotate the mass maps whenever the light-cone diameter exceeds the box size to avoid encountering the same structure multiple times along the line of sight but, at the same time, not unnecessarily erasing correlations along the line of sight. In Appendix A of Broxterman et al. (2024) we found that the rotation prescription had little impact on the final number density of WL peaks. To validate our map construction procedure, we first compare the angular power spectrum of the final WL convergence map to the prediction from

HALOFIT (Takahashi et al. 2020) provided by CLASS (Blas et al. 2011) in Fig. 1. CLASS provides the three-dimensional matter power spectrum ( $P_m$ ), which we relate to the angular power spectrum ( $C(\ell)$ ) using (Limber 1953; LoVerde & Afshordi 2008):

$$C(\ell) = \frac{9H_0^4\Omega_m^2}{4c^4} \int_0^{\chi_{\text{hor}}} d\chi \frac{W^2(\chi)}{\chi^2 a^2(\chi)} P_m\left(\frac{\ell + 1/2}{\chi}, z(\chi)\right), \quad (10)$$

where  $W(\chi)$  is given by equation 5. The HALOFIT + CLASS prediction is given by the black dashed curve. The green solid line shows the estimate using the employed methods in this paper, i.e. assuming the Born approximation and using the HEALPY ANAFAST routine. Finally, the dotted gray curve shows the angular power spectrum generated using the more elaborate backward ray-tracing method used in Broxterman et al. (2024). The bottom panel shows the ratio to the CLASS + HALOFIT prediction. At the power spectrum level, the ray tracing and Born approximation give the same results, as expected (Hilbert et al. 2020). The estimates also agree well with the HALOFIT prediction and illustrate that the map construction algorithm works well. The difference at small scales is caused by the pixelization of the matter field onto the HEALpix grid, as discussed in more detail in Section 3.5 of Broxterman et al. (2024). For a detailed comparison between predictions from HALOFIT and FLAMINGO, see Upadhye et al. (2023).

### 3.2 Weak-lensing peaks

To mimic a *Euclid*-like signal, we smooth the final maps with a Gaussian beam with a smoothing scale of 1 arcmin and we apply galaxy shape noise by drawing from a normal distribution with mean  $\mu = 0$  and standard deviation  $\sigma = \sigma_\epsilon / \sqrt{2n_{\text{gal}} A_{\text{pix}}}$ , where  $\sigma_\epsilon = 0.26$  is the rms total intrinsic ellipticity of the source galaxies,  $n_{\text{gal}} = 30 \text{ arcmin}^{-2}$  is the source galaxy number density and  $A_{\text{pix}}$  is the area of a HEALpix pixel (Kaiser & Squires 1993; van Waerbeke 2000;

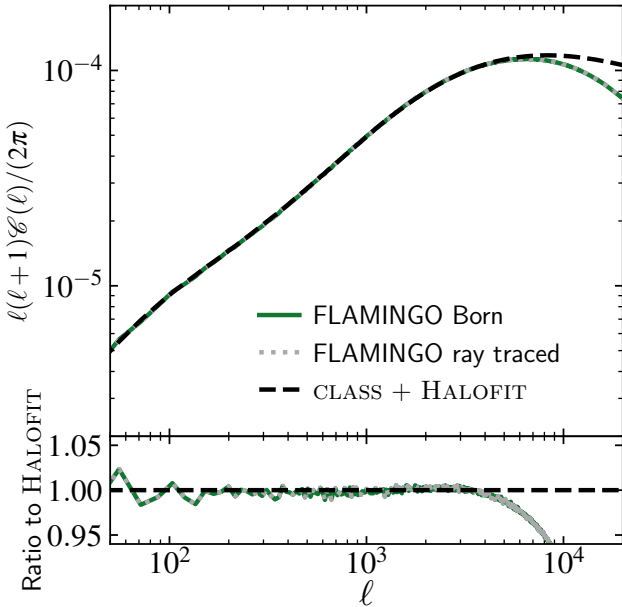


**Figure 1.** Top: Weak lensing convergence angular power spectrum estimated using a *Euclid*-like source redshift distribution, corresponding to the mean of the 8 L2p8\_m9\_DMO observers. The full-sky map is constructed from the FLAMINGO mass maps and assumes the Born approximation (solid green) or a more advanced backward ray-tracing method (dotted gray). The dashed black curve shows the prediction from HALOFIT using the non-linear 3D matter power spectrum provided by CLASS. Bottom: ratio to the CLASS + HALOFIT prediction. The three estimates agree to an excellent degree apart from small scales due to the pixelisation of the HEALpix maps.

**Euclid Collaboration:** Martinet et al. 2019; **Euclid Collaboration:** Ajani et al. 2023; **Euclid Collaboration:** Mellier et al. 2024).<sup>1</sup> By smoothing the maps with different smoothing lengths, information corresponding to different scales may be probed, as illustrated by Li et al. (2019). In this work, we focus on a single smoothing scale but note that the main conclusions of the halo-peak matching are independent of the exact value of the smoothing scale, as illustrated in Appendix A. We define a peak as any pixel on the HEALpix grid with a value greater than those of its 8 nearest neighbors. Although a crude definition, this has been used widely in observations (e.g. Hamana et al. 2015; Shan et al. 2018; Grandón et al. 2024) as well as simulations (e.g. Weiss et al. 2019; Coulton et al. 2020; Davies et al. 2024).

To match the peaks to haloes, we assign two angular coordinates and a redshift to each peak and halo (see also Section 3.3). The positions of the peaks on the HEALpix grid directly provide the angular coordinates of the peaks. To assign a redshift to each peak, we exploit the summation properties of the Born approximation. As explained in Section 3.1.1, the WL signal is estimated with a double summation (equations 7 & 8). The first summation sums over all the lens planes, and for each lens plane, the second summation calculates the contribution of all more distant source planes. For each peak, we determine the redshift of the shell where the contribution from the lens (equation 7) is the largest and assign this redshift to the

peak. Before determining the maxima, we smooth the contributions at each shell with the same smoothing kernel as applied to the final map. We refer to the redshift assigned in this way as  $z_{\text{true}}$  as this is the redshift of the major overdensity that acts as the lens to generate the peak. After matching the peaks to individual haloes, as explained in Section 3.4, the peaks are assigned the redshift of the halo to which they have been matched. In Section 3.5, we will modify these redshifts to account for realistic observational redshift uncertainties.

The straightforwardness with which we can directly assign a redshift to each peak is the main reason why we choose to adopt the Born approximation. Assigning a redshift to a peak is less straightforward using the ray-tracing methodology used in Broxterman et al. (2024), as that approach effectively sums over the contributions of all the sources, instead of the lenses.

### 3.2.1 Purity

To ensure that we select a peak sample that predominantly corresponds to a single halo along the line of sight towards each peak, we apply cuts based on the peak value, applied noise, and most and second most contributing lens shells, all measured at the angular position of the peak. First, if the smoothed random noise alone can account for over 50 per cent of the final peak value, we call this peak a ‘Noise peak’. Second, to guarantee that the object corresponds to a single shell and it is not a result of a superposition of multiple objects along the line of sight, we require the most contributing shell to contribute more than 50 per cent of the final peak value and the second most contributing shell to contribute less than 50 per cent of the most contributing shell. We refer to the subset of peaks satisfying these criteria as ‘Single shell peaks’. These cut will throw away a small subset of haloes located directly on the edge of two subsequent shells, which are, in reality, single haloes. As we aim to get a pure selection of peaks, we do not study these peaks in more detail, but we note that, as a consequence, our resulting selection of Single shell peaks will likely be slightly underestimated. We refer to the remaining set of peaks as ‘Multiple shells peaks’, as their WL convergence cannot be attributed to the applied noise or a single shell, or there are multiple contributing shells along the line of sight.

In Fig. 2, we show the fractional contribution of each of the three peak categories to the total number of peaks as a function of their WL peak convergence value. The top panel corresponds to a *Euclid*-like analysis, whereas the bottom panel corresponds to a Stage III WL survey-like analysis. The top axis of each panel shows the SNR ( $= \kappa/\sigma_{\text{noise}}$ ). The dashed-dotted, dashed, and solid curves indicate the Noise, Multiple shells, and Single shell peaks, respectively. The curves correspond to the mean estimates of the eight observers in L2p8\_m9, but we find the same conclusions apply for the measurement in the DMO runs, i.e. baryonic effects do not change this picture.

Focusing first on the top panel, the highest-valued peaks nearly always belong to the Single shell category, as they are caused by a single overdensity along the line of sight. At  $\kappa < 0.4$  (0.2), the Multiple shells (Noise) peaks become increasingly important. Below SNR = 5 ( $\kappa < 0.11$ ), the Noise peaks dominate the signal. This is expected as the noise value necessary to account for over half of the signal is increasingly less likely to be drawn for higher-valued peaks. For  $\kappa \lesssim 0$  the Noise peak contribution drops again. In Appendix B, we show in more detail that these peaks do not arise from the noise. We find that separating these negative-valued peaks into Single shell and Multiple shells peaks depends strongly on the exact choice of division criterion, which in this case is the ratio of the second to the most contributing shell and the ratio of the most contributing

<sup>1</sup> This noise configuration likely slightly underestimates the actual noise that will be measured by Stage IV WL surveys but we still adopt it to facilitate a consistent comparison with Broxterman et al. (2024).

shell to the final peak value. However, this is only the case for the low- $\kappa$  peaks, and the  $\kappa \gtrsim 0.1$  subset, which contains the WL peaks considered in the remainder of this work, is robustly split into the different categories. The contribution of Multiple shells peaks is  $\sim 10$  per cent at  $\text{SNR} = 5$  and decreases monotonically until it vanishes at  $\text{SNR} = 18$  ( $\kappa = 0.40$ ).

These results agree with those from Hamana et al. (2004) & Yang et al. (2011) who used a different approach but also found that high-signal peaks (in their case  $\text{SNR} > 3.5$ ) principally stem from a single massive halo each. In Fig. 2, we see that their convergence cuts are in the regime where the purity drops steeply as the noise and superposition of multiple objects along the line of sight generate a larger fraction of the peaks for lower  $\kappa$  values. At this point, we have not yet aimed to match individual peaks to haloes, but based on the results of Hamana et al. (2004); Yang et al. (2011); Liu & Haiman (2016), we expect that we should be able to match most of the peaks to a single massive halo each, as we will indeed show in Section 3.4.

To illustrate the major improvement of the Stage IV WL surveys, we compare the *Euclid* predictions to those resulting from using the same methods but assuming Stage III characteristics. The red curves in the bottom panel of Fig. 2 illustrate the same 3 peak categories, but are based on a WL map constructed using the KiDS DR4 (KiDS-1000) source redshift distribution and noise properties (Kuijken et al. 2019; Asgari et al. 2021). The KiDS signal is dominated by Noise peaks to larger  $\kappa$  values, and therefore, fewer peaks can be confidently assigned to a single halo. The main difference rests in the source galaxy background number density, which is a factor  $\approx 5$  greater for *Euclid*, and therefore, the mean noise is a factor  $\approx 2.2$  times greater for the KiDS analysis. Additionally, Stage IV surveys detect more distant galaxies, so the WL signals will also be stronger, while the area of the *Euclid* survey will be  $\sim 10$  times greater, which impacts the total number of measured objects.

Selecting a higher WL convergence cut gives a purer sample as the fraction of Single shell peaks increases. For an  $\text{SNR}$ -cut of 5 (8), we find a purity percentage (percentage of Single shell peaks) of 76 (96) per cent for *Euclid* and 56 (100) per cent for KiDS, assuming a KiDS-like noise such that  $\text{SNR} = 5$  corresponds to  $\kappa = 0.25$  for the latter predictions. We stress that these percentages are likely underestimated due to the conservative cuts we have applied to assign a peak to a category. Not only the purity of the *Euclid* sample is higher at a fixed WL convergence cut, the total number of peaks with  $\text{SNR} > 5$  (8) increases from 140 (4) in the full KiDS footprint ( $\approx 1,500 \text{ deg}^2$ ) to  $5.5 \times 10^4$  ( $6.8 \times 10^3$ ) in the full *Euclid* footprint ( $\approx 14,000 \text{ deg}^2$ ), illustrating the major improvement of Stage IV surveys as they will measure over two orders of magnitude more high-valued peaks. The KiDS estimate is roughly consistent with the recent HSC Y3 analysis results from Chen et al. (2024) and Chiu et al. (2024), who find 129  $\text{SNR} > 4.7$  peaks on the WL aperture mass maps. While their area is smaller than the area we assume for the KiDS-1000 analysis, their survey is deeper, so we expect that their number roughly agrees with our simple KiDS estimate.

We compare our purity prediction to those from Yang et al. (2011). They report a purity of only 20 per cent for  $\text{SNR} > 3.5$  peaks. This is 4 times lower than our purity, but lowering the  $\text{SNR}$  threshold greatly impacts the purity. Assuming their  $\text{SNR}$  cut, we still find a purity of 38 per cent. Their method attributes a peak to a halo by assuming NFW profiles for each simulated halo and calculating the expected convergence signal using this profile. They then match peaks and haloes using a maximum angular separation of 1.8 arcmin. If the estimated WL convergence is more than half the final WL peak value, they attribute the peak to a single massive halo. However, they already note that this approach's estimated WL convergence has a fractional

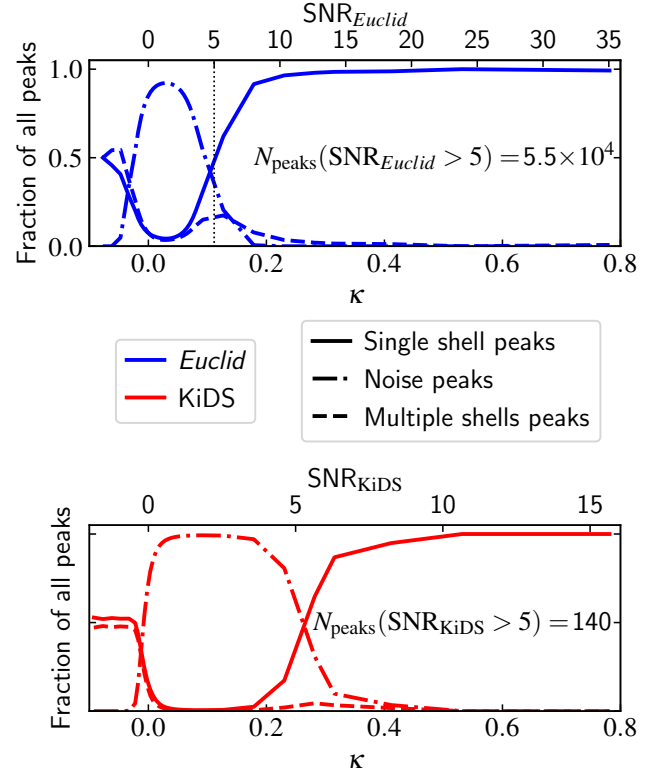


**Figure 2.** Fractional contribution of WL peaks that stem from a single redshift shell ('Single shell', solid), were assigned a random noise that can account for over half of the final peak signal ('Noise peaks', dashed-dotted), or originate from multiple shells along the line of sight ('Multiple shells peaks', dashed) as a function of WL convergence ( $\kappa$ ). The blue and red curves correspond to a *Euclid*- and KiDS-like analysis, respectively. The purity (fraction of Single shell peaks) increases with  $\kappa$ . We apply an  $\text{SNR}$ -cut of 5, as indicated by the vertical dotted line in the top panel, as selection criteria for the remaining analysis. The number of  $\text{SNR} > 5$  peaks estimated for the final data releases of the surveys is indicated in each panel, assuming an area of  $1,500 \text{ deg}^2$  and  $14,000 \text{ deg}^2$ , for KiDS and *Euclid*, respectively. Stage IV WL surveys will resolve a large amount of high-SNR peaks corresponding to massive clusters that could be used to constrain cosmology.

bias of 7 per cent and underestimates the WL convergence values. As we do not make any assumptions about the halo profile and the division criteria differ, some differences between the two approaches are expected. In conclusion, we find similar purity percentages to those in previous work.

Hamana et al. (2004) estimate that the mean number of haloes that cause a WL peak with  $\text{SNR} > 4$  is 37 per  $\text{deg}^2$ . At the same  $\text{SNR}$  cut, we find a lower peak number density of only 11 peaks per square degree. Based on the source redshift distribution, we expect their signal to be stronger than we measure. With their  $\text{SNR}$  cut, they report a contamination rate, i.e. a percentage of peaks that cannot be attributed to a single halo, of 44 per cent. The main difference between their analysis and ours is the choice of  $\text{SNR}$  cut. From Fig. 2 it is clear that the noise and superposition contributions vanish quickly around this  $\text{SNR}$  regime. If we apply their  $\text{SNR}$  cut, we find a similar contamination rate of 47 per cent.

In the remainder of our analysis, we apply an  $\text{SNR}$  cut to our peak sample, as indicated by the dotted black curve in the top panel of Fig. 2. We will only use peaks with an  $\text{SNR}$  value greater than

the cutoff value of  $\text{SNR} = 5$  to determine the redshift evolution and perform the halo-peak matching. We choose this value because at larger  $\text{SNR}$ , Single shell peaks dominate and we thus have a reasonably pure sample. Additionally, we stress that until now, we have been conservative in our noise and multiple shells cuts as we find that most  $\text{SNR} > 5$  peaks belonging to either of these categories still clearly correspond to a single object in the overdensity field, as illustrated in more detail in Appendix C. When studying the redshift distributions of the peaks, we assign a redshift to all Noise and Multiple shells peaks above the  $\text{SNR}$ -cut and include them in the analysis, as in an observational campaign there is no way of deciding which peaks are generated by the noise.

In Broxterman et al. (2024) we argued that, for a similar analysis, using the number density of WL peaks as a function of their WL convergence strength, the  $\kappa = [0.1, 0.4]$  regime is most useful for WL peak inferences, as the differences are most easily interpretable in that range. Lower-valued peaks require accurate modeling of instrument and survey characteristics, while the number of higher-valued peaks is subject to significant cosmic variance. Additionally, for this intermediate regime, the differences between the cosmology and baryonic variations could be easily understood by considering the impact of baryonic physics on single haloes and the impact of different cosmological parameters on the HMF. The peaks belonging to this WL convergence regime are predominantly included in our sample after the  $\text{SNR} > 5$  cut.

### 3.3 Halo light-cone

To match the peaks to haloes, we use the FLAMINGO halo light-cones. FLAMINGO uses a modified version of the public halo finder Hierarchical Bound-Tracing (HBT+) to identify haloes and track their formation and evolution, including mergers (Han et al. 2018, Forouhar Moreno et al. in prep). The halo finder is used to identify central haloes and their most-bound BH particle, which is set as the centre of the halo. The 3-dimensional positions of the haloes are then converted to angular positions and redshifts, as seen by the different virtual observers in the runs, and saved as halo light-cone files. We directly use these files for our halo-peak matching. We rotate the angular coordinates of the haloes using the same rotations as the light-cone mass maps. On top of the halo finder, which determines the centres of the haloes in the simulation, the FLAMINGO data includes a large set of precomputed quantities in Spherical Overdensity APerture (SOAP) catalogues (McGibbon et al. in prep). From the SOAP catalogues, for each halo, we use  $M_{200c}$ , the mass within a spherical aperture with radius  $R_{200c}$  enclosing an average overdensity of  $\langle \rho(z) \rangle = 200\rho_{\text{crit}}(z)$ , of the closest snapshot in redshift.

### 3.4 Halo - peak matching

Using the angular coordinates and redshifts of the peaks and haloes, we now match individual peaks to haloes from the FLAMINGO halo light-cones. We perform the matching separately for each shell.<sup>2</sup> For

<sup>2</sup> We find that allowing a peak to be matched to a halo in the previous or subsequent shells if the haloes are close to the edge of the shell improves a small number of matches. In these cases, on one side of the edge, there is a high-valued WL peak without a corresponding massive halo. On the other side, at the same angular position, there is a massive halo without a corresponding peak. We allow a peak to be matched to haloes that are within 1 cMpc of the shell edge, which corresponds to  $R_{200c}$  of a  $M_{200c} \approx 10^{14} M_{\odot}$  halo. Doubling this value does not significantly change the results.

each shell, we select all peaks corresponding to that shell. As these peaks all have the same redshift (i.e. the central redshift of the shell), their WL kernel (equation 8) is unchanged, and a higher peak should directly originate from a more overdense structure. However, as there may be small variations due to other minor over- or underdense regions within the shell or along the line of sight, the noise that is applied in the end, and because the haloes are not perfectly spherical NFW haloes but differ in shape (e.g. Velliscig et al. 2015; Chua et al. 2019), these peaks will not all correspond to the most massive haloes. Therefore, for each shell, we select the  $N$  most massive haloes such that  $N_{\text{halo}} = 100N_{\text{peak}}$ , which are then allowed to be matched to the peaks. We find that changing this value by a factor of two does not impact the results.

To match the haloes to the peaks, we determine the great circle distance ( $\Delta\theta$ ) between each peak and all nearby haloes. First, we project the haloes onto the HEALPix pixels according to their location on the halo light-cone. Then, using the HEALPY function `QUERY_DISC`, we select all haloes within 2 degrees of the peak. We then calculate the distance between the peak and all haloes in the angular aperture and scale the distances by the quantity  $\theta_{200c} = R_{200c}/d_A$ , which is a proxy for the angular size of the halo on the sky, where  $d_A$  is the angular diameter distance. Then, we select the closest halo in  $\Delta\theta/\theta_{200c}$  for each peak. We do not require a bijective match between the halo and peak as we find that a single halo may cause multiple peaks in the final map, particularly for massive, low-redshift, or merging systems.

Fig. 3 illustrates the accuracy of the matching procedure. The left-hand panel shows a  $10 \times 10$  square degree patch from the final WL convergence map of the virtual observer in L1\_m9 from which the peaks are selected. In this panel, the  $\text{SNR} > 5$  peaks that correspond to the fourth shell ( $z = [0.15 - 0.2]$ ) are indicated by yellow circles. The bright peaks that do not have a circle have been assigned to other redshift shells. The right-hand panel shows the overdensity field of the fourth shell for the same angular region. The field corresponds to a physical size of  $\approx 110 \times 110 \text{ pMpc}^2$ . Each yellow circle assigned to this shell visually corresponds to an overdense structure. The red dotted circles indicate the positions of the haloes to which the peaks have been matched. All peaks and haloes are at almost the same position, indicating the peaks are matched correctly.

Some peaks, such as the one to the left of the legend, have a small angular offset compared to the halo centre. As no other haloes are near the same position, we are still confident that the peaks have been matched to the correct haloes. Minor differences between the halo light-cone coordinates and smoothed projected WL overdensity are expected, as we apply noise and smooth the final maps and because of projection effects. Other structures seemingly equally overdense as the ones that are associated with a WL peak do not have a corresponding peak. Most of these structures cause a peak in the final WL convergence map with an  $\text{SNR}$  value below the cut-off value we apply, as illustrated in Appendix C. Alternatively, a peak at that position has been assigned to a more strongly contributing structure along the line of sight. As we chose to keep the peak catalogue relatively pure, we do not aim to include these peaks in this analysis. Still, we stress that the  $\text{SNR}$  cut we applied has not been optimised and may be lowered to include more peaks, albeit at the cost of purity.

In Appendix C, we split the peaks in Fig. 3 into the three categories considered in this work (i.e., Single shell, Noise, and Multiple shells peaks). There, we show that, generally, Noise and Multiple shells peaks are still clearly assigned to a massive halo. In that appendix, we also show the  $3 < \text{SNR} < 5$  peaks that were assigned to this shell and illustrate that most overdense structures that do not have a corresponding peak in Fig. 3 generate a peak with an  $\text{SNR}$ -value below the cut that we apply.

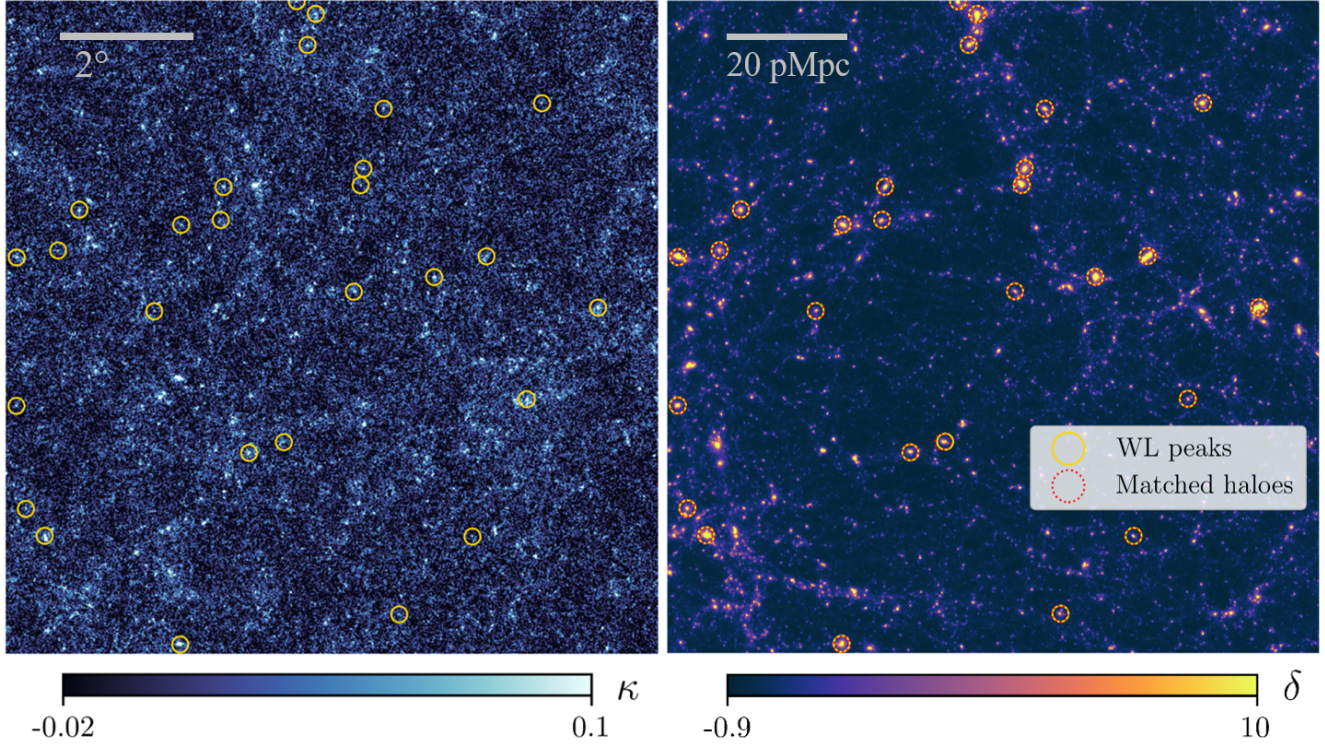


**Figure 3.** Left:  $10 \times 10 \text{ deg}^2$  patch of the *Euclid*-like WL convergence field of the virtual observer in L1\_m9. The WL peaks are selected from this map. The  $\text{SNR} > 5$  peaks that are assigned to the fourth shell ( $z = [0.15 - 0.2]$ ) are indicated by the yellow circles. Right: projected overdensity field of the fourth shell of the same angular field, corresponding to a physical size of  $\approx 110 \times 110 \text{ pMpc}^2$ . The yellow circles correspond to large overdensities. Red dotted circles show the positions of the haloes to which the peaks are matched. Most of the visibly overdense structures with no associated peak generate a peak with a lower SNR-value than the cut we apply, as illustrated in Appendix C.

### 3.5 Observed redshifts

Until now, we have used the simulation properties to identify structures with high precision and accuracy at any point in space and time within the simulation. However, as observations typically assign a redshift based on a limited number of photometric bands, we explore how the expected associated observational uncertainties impact our results.

*Euclid* will rely on photometric redshifts for the bulk of the measured galaxies. The survey requirement is to measure the photometric redshifts such that the standard deviation on the uncertainty satisfies  $\sigma_z < 0.05(1 + z)$  with a catastrophic failure rate of less than 10 per cent (Euclid Collaboration: Mellier et al. 2024). However, the peaks we measure correspond to the most massive clusters, as we will show in Section 4.1, which will likely contain bright and red objects that will be easier to identify using either the regular methodology or a red-sequence cluster identification mechanism such as redMaPPer (Rykoff et al. 2014). Therefore, assuming the general *Euclid* requirement will overestimate the redshift uncertainty on our peak sample. The assumption that the WL peaks can be associated with optical clusters using red-sequence-based cluster finders is confirmed by the recent HSC Y3 analysis of Chen et al. (2024) and Chiu et al. (2024), who find that they can match all their  $\text{SNR} > 5$  peaks selected from aperture mass maps to an existing measurement of an optical cluster from CAMIRA (Oguri et al. 2018), redMaPPer or WHT (Wen & Han 2015).

The *Euclid* satellite will measure photometry in 1 visual ( $m_{\text{VIS}}$ ) and 3 near-infrared ( $YJH$ ) bands, but the photo- $z$  measurements

will strongly rely on ground-based photometry. The satellite's measurements will be complemented by 6 ground-based photometric measurements in the  $ugrizy$  bands from a range of different facilities (Euclid Collaboration: Pocino et al. 2021; Euclid Collaboration: Mellier et al. 2024). As a more accurate estimate of the redshift uncertainty, we take as a reference the KiDS bright sample, which is a bright subsample of  $\sim 10^6$  galaxies of KiDS-1000 that uses the 9-band  $ugriZYJHK_s$  photometry to determine photo- $z$ s (Kuijken et al. 2019; Bilicki et al. 2021). By comparing to the GAMA spectroscopic redshifts, they find they assign photo- $z$ s to the bright subsample with an accuracy of  $\sigma_z = 0.018(1 + z)$  up to  $z = 0.5$  without catastrophic failures. Vakili et al. (2023) select a KiDS-1000 subsample using a red sequence template that includes estimating the red sequence redshifts, and by comparing to spectroscopic redshifts, they find similar accuracy and precision as the KiDS bright sample extending up to  $z = 0.8$ .

As the number of bands and depth used for the *Euclid* photometric redshift estimates will be similar to KiDS, we expect that the photometric redshifts for the clusters that correspond to our WL peaks will be measured with similar accuracy and precision as the KiDS bright sample. To mimic the observed redshifts, for each  $z_{\text{true}}$  that has been assigned to a peak, we therefore draw an observed redshift according to a normal distribution with mean  $\mu$  and standard deviation  $\sigma$ ,

$$\mathcal{N}\left\{\mu = z_{\text{true}}, \sigma_z = 0.02(1 + z_{\text{true}})\right\}, \quad (11)$$

which is truncated at  $z = 0$ . We will only show the redshift distributions of all the baryonic and cosmology variations as a function of the

mock photometric redshifts  $z_{\text{obs}}$ . Still, we note that the same conclusions hold if we instead use the true redshifts or modify the redshifts with an uncertainty of  $\sigma_z = 0.05(1 + z_{\text{true}})$  and an extreme outlier fraction of 10 per cent, to the degree of the *Euclid* requirements.

## 4 RESULTS

We now present the results of the halo peak matching by showing the WL peak distribution binned by halo mass in Section 4.1. We then quantify the completeness of the matched haloes in Section 4.2 and study the redshift distribution of the WL peaks in Section 4.3. We quantify the degree of numerical convergence and cosmic variance in Sections 4.3.1 and 4.3.2, respectively. Finally, we qualitatively and quantitatively compare the difference between the cosmological and baryonic impact on the peak statistics in Sections 4.4 and 4.5.

### 4.1 Peak distribution in halo mass

First, we show the results of matching the haloes to peaks by binning the peaks by halo mass. Fig. 4 shows the number density of WL peaks as a function of WL convergence for all redshifts combined. The top x-axis shows the SNR for the *Euclid*-like analysis. The solid black curve gives the distribution of all peaks measured in L1\_m9. The SNR  $> 5$  selection, which primarily corresponds to a single halo per peak, is binned by the halo masses of the haloes to which the peaks have been matched, as depicted using increasingly darker colors for the larger halo mass bins. The figure also shows the Noise peaks (dot-dashed) and Multiple shells peaks (dashed), as detailed in Section 3.2. The fraction of Noise peaks decreases with increasing WL convergence. At SNR = 5, the Noise peaks account for  $\sim 10$  per cent of all peaks, but this quickly decreases to 0 at SNR = 10 (see also Fig. 2).

The bottom panel of Fig. 4 shows the fractional contribution of all mass bins. As expected, we find that, on average, higher-valued WL peaks correspond to more massive haloes. We find qualitatively similar results to Hamana et al. (2004); Yang et al. (2011); Liu & Haiman (2016), who found SNR  $> 3.5$  peaks are predominantly caused by a single massive halo each. We can now study the peaks as a function of their halo mass in more detail. For  $\kappa > 0.25$ , we find that over 95 per cent of the peaks can be attributed to haloes with  $M_{200c} > 10^{14} \text{ M}_\odot$ . Of all SNR  $> 5$  peaks, the majority are matched to haloes with  $M_{200c} = 10^{14} - 10^{14.5} \text{ M}_\odot$ . In Broxterman et al. (2024), we already hypothesised that the WL peaks originate primarily from  $M_{200c} > 10^{14} \text{ M}_\odot$  haloes based on the differences between the thermal and kinetic jet AGN variations and the comparison of the HMFs of these runs. We now confirm this hypothesis.

Liu & Haiman (2016) used observational data from the CFHTLens survey to link haloes to WL peaks. They found that each peak with SNR  $> 3.5$  corresponds to a single halo of  $M_{\text{vir}} \sim 10^{15} \text{ M}_\odot$ . Qualitatively, this agrees with our findings as their analysis probes less deep, but our highest-valued  $\kappa$  peaks are dominated by haloes with  $M_{200c} > 10^{15} \text{ M}_\odot$ .

### 4.2 Completeness

We define completeness as the fraction of haloes within a halo mass bin matched to at least one WL peak over the total number of haloes in that bin. Fig. 5 shows the completeness as a function of redshift and binned by halo mass. The solid curves correspond to haloes matched to peaks with SNR  $> 5$ , and the dashed curves include only those matched to SNR  $> 8$  peaks. The cumulative completeness up to  $z =$

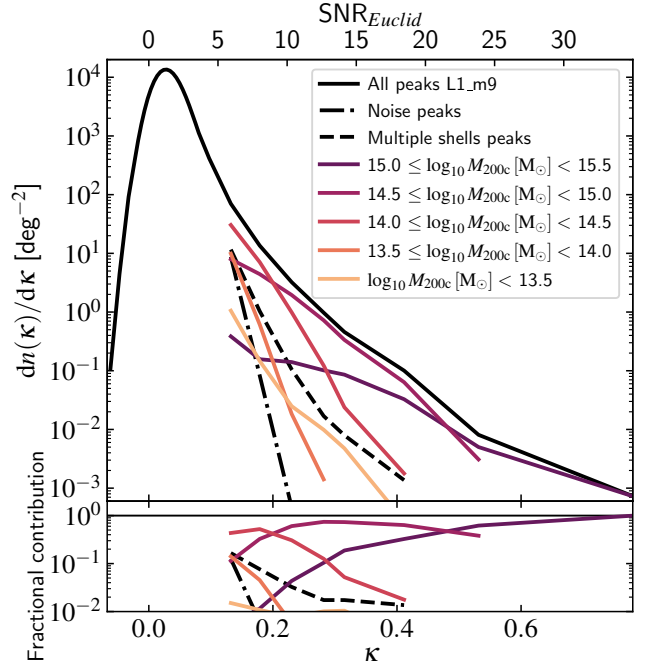


**Figure 4.** Top: number density of WL peaks as a function of WL convergence (bottom x-axis) and SNR (top x-axis) for the virtual observer in L1\_m9 (solid black). Noise and Multiple shells peaks are indicated by black dashed-dotted and dashed curves, respectively. Peaks with  $\text{SNR} > 5$  are binned by  $M_{200c}$  of the haloes to which they have been matched, with larger mass bins indicated by increasingly darker solid curves. Bottom: fractional contribution of all mass bins to the total number of haloes. The high-valued ( $\kappa > 0.11$ ;  $\text{SNR} > 5$ ) WL peaks primarily trace haloes with  $M_{200c} > 10^{14} \text{ M}_\odot$ .

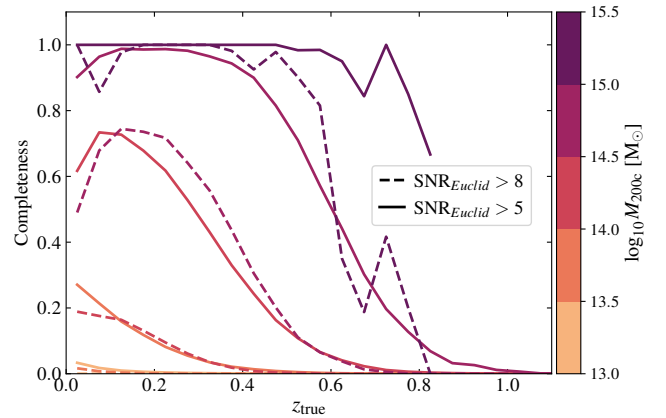


**Figure 5.** The completeness, i.e. the fraction of haloes matched to a high-valued WL convergence peak, as a function of the halo redshift. The haloes are binned by  $M_{200c}$ , and more massive halo mass bins are shown in increasingly darker colors. The solid curves correspond to the fiducial  $\text{SNR} > 5$  sample, while the dashed curve only selects haloes matched to peaks with  $\text{SNR} > 8$ . The completeness drops for lower masses and higher redshifts. The impact of the smoothing scale on the completeness is studied in more detail in Appendix A.

**Table 2.** The completeness, i.e. the fraction of haloes matched to an  $\text{SNR} > 5$  WL peak, assuming a smoothing scale of 1 arcmin. This peak sample has a purity of 76 per cent (see Fig. 2). The columns list the halo mass bin,  $M_{200c}$ ; the total number of haloes per  $\text{deg}^2$  on the entire halo light-cone until  $z = 3$ ; completeness up to  $z = 0.5$  and 1.0.

$\log_{10} M_{200c} [\text{M}_\odot]$	No. haloes [ $\text{deg}^{-2}$ ]	Completeness $z < 0.5$	Completeness $z < 1.0$
13.0 – 13.5	$8.9 \times 10^2$	0.002	0.001
13.5 – 14.0	$1.6 \times 10^2$	0.038	0.010
14.0 – 14.5	$1.9 \times 10^1$	0.378	0.136
14.5 – 15.0	$1.2 \times 10^0$	0.930	0.578
15.0 – 15.5	$2.3 \times 10^{-2}$	1	0.984

0.5 and 1.0 for haloes matched to  $\text{SNR} > 5$  peaks is given in Table 2. The table also includes the total number of haloes per square degree on the halo light-cone until  $z = 3$ . We find excellent completeness for the most massive haloes. Of all 929  $M_{200c} > 10^{15.0} \text{ M}_\odot$  haloes, 98 per cent has been matched to an  $\text{SNR} > 5$  peak. Up to  $z = 0.5$ , this fraction is 100 per cent. Of all  $5.0 \times 10^4 M_{200c} = 10^{14.5} - 10^{15.0} \text{ M}_\odot$  haloes, 52 per cent has a corresponding  $\text{SNR} > 5$  peak. Until  $z = 0.5$ , this is 93 per cent. At higher redshifts, as well as for lower masses, the completeness drops. This is expected, as lower mass objects, on average, generate weaker WL signals, higher-redshift objects have fewer source galaxies to lens, and the contribution of the WL kernel decreases at larger redshifts.

For the  $10^{14} < M_{200c} [\text{M}_\odot] < 10^{15}$  bins, we predict decreasing completeness at low redshift ( $z < 0.2$ ), which can be attributed to the fixed smoothing scale that is applied. For some of these objects, the smoothing scale is too small to achieve the optimal SNR, as they subtend a larger angular scale than is smoothed over. We illustrate this in more detail in Appendix A, where we show the completeness increases for these low-redshift bins when adopting a larger smoothing scale. The most massive haloes are so massive that they are matched to a WL peak independent of the smoothing scale we use. As the redshifts of the peaks are not known before detecting them, a smoothing scale has to be chosen without considering that information. The adopted smoothing scale is a trade-off between higher completeness at lower or higher redshifts for a larger or smaller smoothing scale than the fiducial value adopted in this work, respectively. We adopt a 1 arcmin scale to facilitate the comparison with Broxterman et al. (2024), but multiple scales may be combined to extract more information (Liu et al. 2015).

The dashed curves in Fig. 5 illustrate that the completeness drops when choosing a higher SNR threshold for the WL peaks. The increase in SNR-cut impacts the completeness of the most massive bin the least, as these haloes generally cause the highest-valued WL peaks.

Hamana et al. (2004) report their completeness in terms of the signal expected for a halo of mass similar to that in their simulation, but with an NFW profile instead of the actual profile of the halo they study. They report a completeness of 81 per cent for haloes with  $\text{SNR}_{\text{NFW}} > 5$ . In our analysis, instead, we illustrate the completeness binned by halo mass. However, at the same time, they reported an efficiency, i.e. a purity, of 82 per cent using this  $\text{SNR}_{\text{NFW}}$  cut. We find similar, although slightly better, values based on our methodology. Combined with the purity shown in Fig. 2, we find that an  $\text{SNR} > 5$  cut will result in a pure sample (76 per cent) while measuring a large number of peaks ( $5.5 \times 10^4$ ). We repeat that extending this to lower SNR is likely possible, as we find that most Noise and Multiple shells peaks are still attributable to a massive object.

#### 4.2.1 Comparison to X-ray and SZ cluster abundance inferences

Next, we compare our completeness to the state-of-the-art X-ray survey eROSITA. Ghirardini et al. (2024) use the cosmology subsample of the X-ray selected eRASS1 cluster sample in their cluster abundance inference. Their sample, consisting of 5,263 clusters on  $\sim 13,000 \text{ deg}^2$ , has an estimated purity of 94 per cent (Bulbul et al. 2024). In our analysis, we find that an  $\text{SNR} > 8$  WL peak sample, corresponding to  $\sim 6,800$  WL peaks for *Euclid* DR3, has a purity of 96 per cent, illustrating that WL peaks are competitive with state-of-the-art X-ray cluster cosmology inferences. Lowering the SNR cut to 5 results in an even greater difference in the number of probed clusters, as  $N_{\text{peaks}}(\text{SNR} > 5) = 5.5 \times 10^4$ , but this is at the cost of the purity which decreases to 76 per cent. Comparing our completeness to that of the eROSITA sample reported in Appendix D of Ghirardini et al. (2024), we see that at  $z = 0.3$ , their sample is  $\approx 100$  per cent complete for  $M_{500c} > 10^{15.2} \text{ M}_\odot$ . At the same redshift, as illustrated in Fig. 5, we find our sample (with an  $\text{SNR} > 5$  cut) similarly complete for  $M_{200c} > 10^{14.5} \text{ M}_\odot$ . For  $\text{SNR} > 8$ , at a similar redshift, our sample has a similar completeness level for  $M_{200c} > 10^{15.0} \text{ M}_\odot$ . For  $z > 0.6$ , the completeness of our WL peak sample drops steeply as a consequence of the WL kernel, even for the most massive haloes.

We also compare our results to the SZ selected samples from Hilton et al. (2021). Their sample consists of 4,195 optically confirmed clusters over  $\sim 13,000 \text{ deg}^2$  extending up to a redshift of 1.9. At  $z = 0.5$ , they report a completeness of 90 per cent down to masses of  $M_{500c} > 3.8 \times 10^{14} \text{ M}_\odot$ , which decreases for lower and higher redshifts as well as for lower masses. They expect 34 per cent of their candidates to be false positives, corresponding to a purity of 0.66. For  $z > 0.6$ , the completeness of their SZ-selected sample is generally better, whereas our WL sample has better completeness for lower redshifts.

To conclude, the  $\text{SNR} > 5$  WL peak sample that Stage IV WL surveys will measure corresponds to massive clusters and has a purity and completeness equal to or better than state-of-the-art X-ray or SZ cluster abundance inferences. This especially holds for redshifts up to  $z \approx 0.7$  and may be improved further by combining smoothing scales as illustrated in Appendix A. At the same time, WL peaks circumvent some of the selection effects and model assumptions, as both SZ and X-ray analyses require assumptions on the parametric form and scatter in the scaling relation relating the observable to the halo mass. Compared to an X-ray or SZ cluster analysis, the limiting factor of this analysis is that the WL kernel restricts the accessible redshift range. Therefore, the redshift range that we probe does not extend to as high a redshift as is probed by X-ray or SZ cluster analyses. In Section 4.1 we have shown that the  $\text{SNR} > 5$  peaks probed by stage IV WL surveys primarily trace  $M_{200c} > 10^{14} \text{ M}_\odot$  haloes. Physically, these correspond to massive clusters of galaxies that should be visible in the optical, SZ, and X-ray (e.g. Allen et al. 2011). The analysis of this paper could, therefore, possibly be extended by including SZ-selected clusters for higher redshifts (e.g. Bocquet et al. 2023, 2024).

### 4.3 Redshift distribution of $\text{SNR} > 5$ WL peaks

In this section, we study the redshift distribution of the  $\text{SNR} > 5$  WL peaks. We stress that all  $\text{SNR} > 5$  peaks, including the Noise and Multiple shells peaks, are assigned a redshift. First, we show the number density of WL peaks binned by redshift. We then investigate the degree of numerical convergence and cosmic variance. Finally, we study the redshift distributions as a function of mock photometric

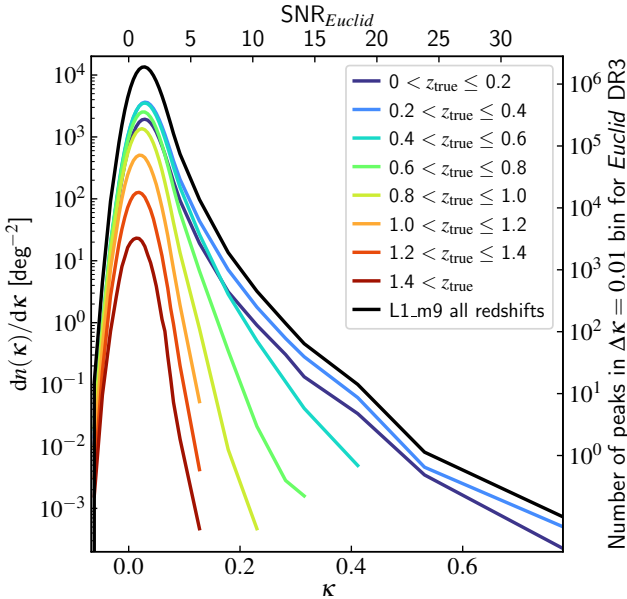


**Figure 6.** Number density of WL peaks as a function of WL convergence binned by redshift for L1\_m9. The redshift is assigned by identifying the lensing plane that contributes most to the final WL peak convergence value (Equation 7). The redshift distribution is determined by the WL kernel, which is set by the source redshift distribution, and the evolution of structure formation. The distribution peaks at  $z = [0.2-0.4]$  as expected from the WL kernel peaking at  $z \approx 0.375$ . The right axis indicates the number of WL peaks in a  $\Delta\kappa = 0.01$  bin for *Euclid* DR3.

redshifts to quantify the impact of baryonic physics and cosmology using the different FLAMINGO 1 cGpc variations.

Fig. 6 illustrates the number density of WL peaks as a function of WL convergence binned by their redshift. The right-hand axis shows the number of peaks that we estimate will be detected in a  $\Delta\kappa = 0.01$  bin in the final *Euclid* data release. As explained before, the redshift distribution of high- $\kappa$  WL peaks depends on the evolution of structure formation and on the WL kernel set by the source galaxy redshift distribution. However, it is also sensitive to cosmology due to the comoving volume-redshift relation. Therefore, the WL peak distributions contain both geometrical and perturbative information.

Fig. 6 illustrates that, generally, there are no peculiar features in the  $\kappa$  distribution of the peaks with different redshifts other than overall amplitude differences. We find that peaks are more likely to be generated from lower redshift bins (particularly  $z = [0-0.6]$ ), as this is where most of the structure has formed and the WL kernel peaks for the *Euclid*-like source distribution, independently of the WL convergence value. Only the lowest redshift bin,  $z = [0-0.2]$  (dark blue), shows different behaviour, as it contains fewer  $\kappa \lesssim 0.15$  peaks than in the  $z = [0.4-0.6]$  and  $[0.6-0.8]$  bins, but for larger WL convergence values, it has more peaks. This characteristic originates from a subset of the high-mass haloes at low redshifts that generate multiple WL peaks. As discussed in the previous section, at low redshifts, the applied smoothing scale is smaller than the angular scale subtended by the most massive objects. These objects may therefore generate multiple peaks, which is reflected in Fig. 6 as the lowest redshift bin, compared to the  $z = [0.4-0.8]$  bins, contains more high-valued WL peaks but fewer low-valued peaks. This behaviour may be avoided by requiring a minimal angular distance between different WL peaks entering the catalog, an effect not dissimilar to fiber collisions.

#### 4.3.1 Numerical convergence

We now establish the degree of numerical convergence by comparing the redshift distributions as measured for the observers in the simulations with different resolutions and box sizes in the FLAMINGO suite. In Fig. 7, we show the signals measured for the L1\_m8\_DMO (red), L1\_m9\_DMO (green), L1\_m10\_DMO (yellow), and the mean of the eight L2p8\_m9\_DMO (blue) observers. The lower (m10) and higher (m8) resolution runs have, respectively, 8 times fewer and more particles than m9 in the same volume and with the same initial conditions. We illustrate the redshift distributions as the number density of the redshifts of WL peaks  $dn(z)/dz$ , i.e. the counts per redshift bin over the bin size ( $\Delta z = 0.05$ ).

The distributions peak at  $z \approx 0.3$  but are moderately flat across the  $z = 0.2 - 0.4$  range. Whereas the WL kernel already peaks at  $z \approx 0.375$ , more massive structures continue to form at low  $z$ , effectively pulling the distribution to lower redshifts than if we had only considered the WL kernel. The bottom panel shows the ratio compared to L1\_m9\_DMO, with the gray band indicating the Poisson error. The observers in the L1 boxes are located at the same position, and these boxes have the same initial phases. Therefore, comparing these three variations directly shows the degree of numerical convergence with the particle mass and spatial resolution. We find a similar degree of convergence as the number density of WL peaks in Broxterman et al. (2024). The m10 run shows a systematic offset of a few per cent for  $z = [0, 0.7]$ . As the simulations are initiated with the same phases and based on the convergence of the HMFs of these runs (see fig. 19 of Schaye et al. (2023)), we expect the same massive haloes to exist in the different variations. Because the WL peak sample primarily probes these massive haloes (see Fig. 4), we do expect that the  $SNR > 5$  haloes probed by L1\_m9\_DMO should still be well resolved in L1\_m10\_DMO. The small but systematic suppression of the L1\_m10\_DMO signal shows that the convergence is slightly worse than the convergence of the HMF, which may be a consequence of halo profiles being less resolved and the peak height in the lower resolution simulation not making the  $SNR > 5$  cut. The convergence between L1\_m9 and L1\_m8 is much better. There is a 5 per cent difference for the lowest redshift bin, which decreases and remains within 1 per cent up to  $z = 0.7$ .

The L2p8\_m9 and L1\_m9 boxes differ in the realization of the initial conditions. Therefore, they are also impacted by cosmic variance and illustrate the convergence with the volume probed. The convergence with box size is slightly worse than with resolution but still within 3 per cent for  $z = 0.1 - 0.8$  and within 1 per cent until for  $z = 0.25 - 0.50$ , where the distribution peaks. In general, the difference is similar to the Poisson error for L1\_m9.

Whereas Fig. 7 shows the numerical convergence for the signal measured in the DMO boxes, we note that the same conclusions apply to the signals measured in the full hydrodynamical simulations.

#### 4.3.2 Cosmic variance

Using the eight different observers in the L2p8\_m9\_DMO box, we test the impact of cosmic variance on our statistics. Again, we show the results for the observers in the DMO run, but we find that the level of difference is the same for the observers in the hydrodynamical simulation. Fig. 8 shows the redshift distribution of  $SNR > 5$  WL peaks for the eight virtual observers. The distributions depend on the specific orientation of the individual observer with respect to the most massive haloes in the simulation. The bottom panel shows the ratio of the distribution for each observer to the mean of the eight observers. The degree of cosmic variance is of the same level as the

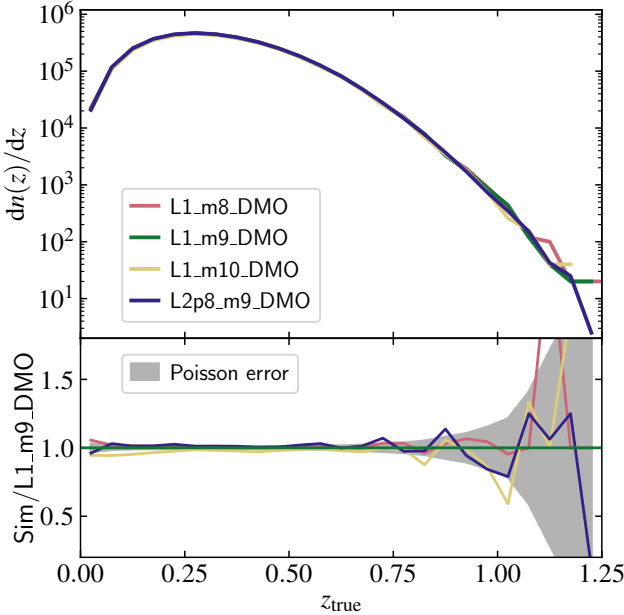


**Figure 7.** Top: number density of the redshifts of  $\text{SNR} > 5$  WL peaks for L1\_m8\_DMO (red), L1\_m9\_DMO (green), L1\_m10\_DMO (yellow), and the mean of the eight observers in L2p8\_m9\_DMO (blue). Bottom: Ratio to L1\_m9\_DMO. The gray band indicates the Poisson error. The agreement between the variations shows good convergence of the L1\_m9 simulations with box size and resolution.

Poisson noise, as shown in the bottom panel of Fig. 7. The effect is less than 1 per cent for  $z = 0.1 - 0.6$ .

#### 4.4 Baryonic and cosmology impact

Next, we compare the distributions of the virtual observers in the 1 cGpc simulations with different levels of baryonic feedback or cosmologies. We emphasize that all observers in the L1 boxes are located at the same position and that the simulations were initiated with the same initial phases. All  $\text{SNR} > 5$  peaks in the final WL convergence maps are assigned the redshift of the lens plane that contributes most to the WL peak convergence value. At each lens plane, the WL peaks are matched to individual haloes and we assign the redshift of the haloes to the peaks.<sup>3</sup> We then adjust the redshifts to account for the expected uncertainty for the massive objects we probe (equation 11). In Fig. 9, we show the ratio of the redshift distributions ( $dn(z)/dz$ ) of the WL peaks of all L1 variations with respect to L1\_m9 (the green curve in Fig. 7) as a function of the perturbed observed redshifts  $z_{\text{obs}}$ . However, we have found that the same conclusions hold when not including any observational redshift uncertainty or catastrophic outliers to the degree of the *Euclid* requirements. We bin the distributions using  $\Delta z = 0.1$ .

<sup>3</sup> The FLAMINGO halo light-cones for L1\_m9\_DMO and the decaying dark matter variations are currently unavailable. We, therefore, show the results of these variations using the central redshifts of the shells to which the peaks have been assigned. As we only show relative differences to L1\_m9, we also restrict the L1\_m9 shell redshifts when comparing to L1\_m9\_DMO, PlanckDCDM12 and PlanckDCDM24. We confirmed that the ratio to L1\_m9 is the same for the simulation variations that do have halo light-cones.

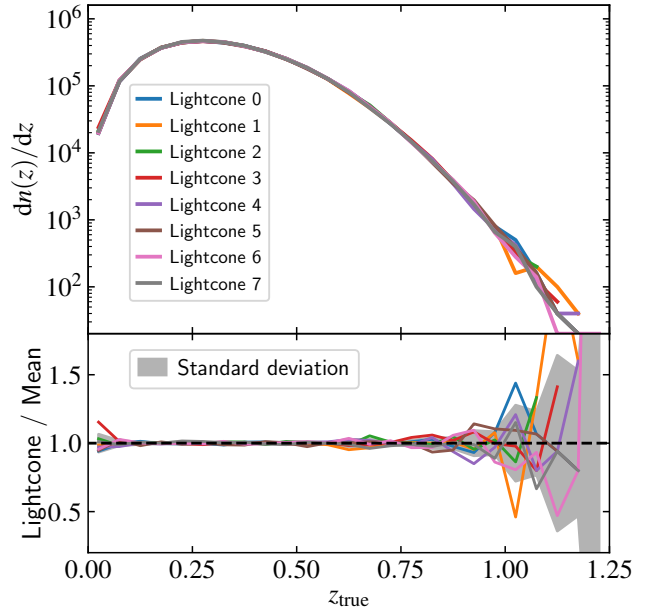


**Figure 8.** Top: number density of the redshifts of  $\text{SNR} > 5$  WL peaks for the eight virtual observers in L2p8\_m9\_DMO. Bottom: ratio to the mean redshift distribution viewed by the eight observers. The standard deviation in the bottom panel, shown by the gray-shaded region, estimates the effect of cosmic variance.

The green shaded region indicates the Poisson error for the expected number of peaks in *Euclid* data release 1 (DR1,  $\sim 2,500 \text{ deg}^2$ ) and for the final data release (DR3,  $\sim 14,000 \text{ deg}^2$ ). The Poisson errors overestimate the differences between the simulation variations as all L1 variations were initiated with the same initial phases, and we thus expect the simulations to be correlated.

The left and central panels show the predictions for L1\_m9\_DMO and the baryonic feedback variations. These variations do not show a different redshift evolution from the fiducial L1\_m9 model as all baryonic curves are close to horizontal, which even holds for the strongest feedback model, fgas- $8\sigma$ . The systematic offsets in amplitude between the curves stem from the fact that the total number of peaks above the SNR cut differs between the simulations. In simulations with stronger feedback, an individual halo that acts as a lens has less mass (e.g. Velliscig et al. 2014). Therefore, the WL convergence value of the peak corresponding to that halo will be lower. As we apply a fixed SNR cut, we expect the total number of peaks to be smaller in simulation with stronger feedback, as was shown in Broxterman et al. (2024) and is reflected in the vertical offsets in Fig. 9.

After correcting for the amplitude difference, all deviations from the shape of the fiducial redshift evolution are within a couple of per cent, though the amplitude of the distributions varies by  $\sim 10$  per cent. The most distinct baryonic variations are L1\_m9\_DMO and Jet. The DMO prediction shows a minor decrease for  $z < 0.2$ . However, when quantifying the difference between the distributions in the next Section, we still find the two distributions are statistically similar. The Jet model was calibrated to the same observables as L1\_m9, and the only difference is the subgrid implementation of AGN feedback. At  $z = 0$ , Jet shows some enhancement compared to L1\_m9, which decreases for higher  $z$ , and at  $z > 0.3$ , the kinetic and thermal AGN feedback variations give the same result. The comparison indicates some dependence on the simulation’s AGN

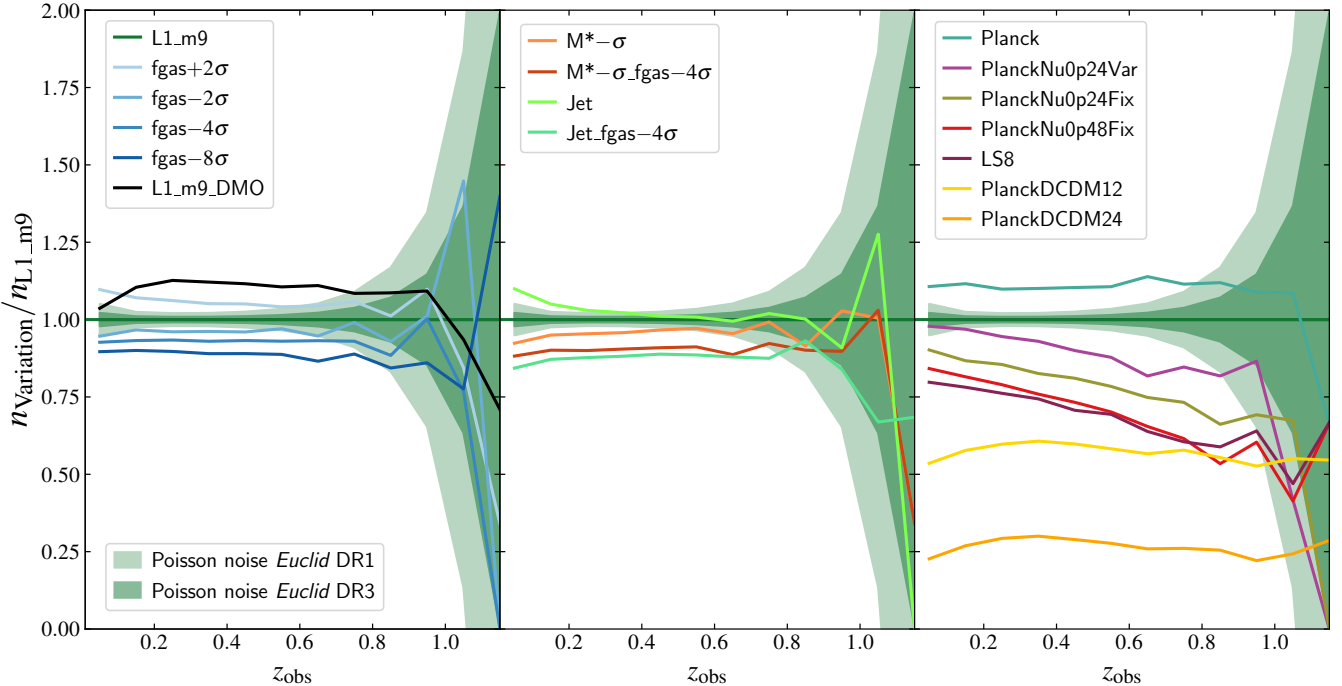


**Figure 9.** Ratio of the redshift distribution of the WL peak number density relative to the prediction for L1\_m9 (green curve in Fig. 7). The left panel includes the variations varying the gas fractions in clusters, with more suppressed gas fractions indicated by an increasingly darker blue color and the DMO signal in black. The middle panel shows the remaining baryonic variations with a different AGN model ('Jet') or a suppressed galaxy stellar mass function ('M\* -  $\sigma$ '). The right panel shows the cosmology variations, including multiple variations using more massive neutrinos or decaying dark matter ('DCDM'). The shaded green regions indicate the expected Poisson uncertainty on the *Euclid* DR1 and DR3 measurements. The baryonic variations (left and central panels) show little change in the shape of the redshift distribution compared to the fiducial model, while some of the cosmology variations, particularly the more massive neutrino variations and LS8, show a different shape redshift evolution. The cosmology variations also show a greater overall offset than the baryonic variations. The shape of the redshift distribution of high-SNR WL peaks is insensitive to the intensity of baryonic feedback, but is sensitive to cosmological parameters, making it potentially valuable for cosmological inference.

subgrid physics model. Comparing the  $z = 0$  HMFs of L1\_m9 and Jet as shown in Fig. 20 of Schaye et al. (2023), we observe that the Jet model, compared to L1\_m9, has a few per cent more haloes of mass  $M_{200c} = 10^{13} - 10^{14} M_{\odot}$ . This excess of haloes could explain the overabundance of WL peaks we observe at low  $z$ .

The lack of differences in the redshift evolution between the baryonic feedback variations shows that the redshift distribution of the high-SNR WL peaks is set by the formation time of massive haloes and is insensitive to the strength of the baryonic feedback that manifests itself primarily at a later stage. As the shape of the L1\_m9\_DMO redshift evolution is consistent with that for the hydrodynamical simulations assuming the same cosmology, the redshift evolution of the WL peak sample studied in this work may be modeled with  $N$ -body simulations only.

Instead, if we focus on the cosmology variations in the right panel, we see greater differences in amplitude and evolution. We distinguish two subgroups in this panel. The first group, consisting of the neutrino mass variations and LS8, shows a different redshift evolution compared to the runs using the fiducial cosmology. Neutrinos act as a form of hot DM, thereby suppressing structure formation (e.g. Lesgourgues & Pastor 2006). This is reflected in the lower value of  $\sigma_8$ , as shown in the next to last column in Table 1. LS8, which has a lower value of  $\sigma_8$  by design, and the higher neutrino mass variations have a lower value of  $\sigma_8$  than the fiducial cosmology. Consequently, there are fewer massive haloes in these simulations. This difference in the number of massive clusters in these simulations, compared to

L1\_m9, increases with redshift. This is also reflected in the redshift distributions, as those belonging to the more massive neutrino and LS8 variations are increasingly more suppressed at higher  $z$ .

The second group, consisting of the Planck and decaying dark matter models, shows no strong difference in the redshift evolution compared to L1\_m9. The *Planck* cosmology has a 3.3 per cent higher value of  $\Omega_m$  and only a 0.6 per cent lower value of  $\sigma_8$ . Considering the HMF, larger values of  $\Omega_m$  increase the overall amplitude of the HMF, whereas a lower  $\sigma_8$  moves the exponential drop to lower halo masses (e.g. Xhakaj et al. 2024). Assuming all peaks emanate from a single halo, we expect the *Planck* and L1\_m9 (i.e. DES Y3 '3 × 2pt + All Ext.') to differ primarily in the total number of haloes as the difference in  $\Omega_m$  is a factor 5 greater than the difference in  $\sigma_8$ . This is reflected in the redshift distributions, as the *Planck* model has more peaks overall, but there is no apparent difference in the redshift evolution. However, more variations should be compared to investigate the impact of different cosmological parameters on the WL peak redshift evolution.

In the DCDM variations, each dark matter particle, independent of its velocity or local density, loses part of its mass as set by the decay rate indicated in the final column of Table 1. The half-life of these models is relatively short compared to values that have already been ruled out by geometrical constraints from the BAO (e.g. Aubourg et al. 2015), but the variations can still be used to understand the impact of decaying dark matter qualitatively. As the DM decays, the total matter density decreases, as indicated in the 9th column of Ta-

ble 1, and the growth of structure formation slows down (e.g. Aoyama et al. 2014; Enqvist et al. 2015). This is reflected in Fig. 9 as the suppression of the PlanckDCDM12 and 24 models is, respectively, a factor 2 and 3 greater than for the other variations. The decaying dark matter models are variations on the Planck model, so we expect them to converge back to Planck at high redshift. Whereas visually the DCDM models do not show large differences from L1\_m9, in the next Section, we will quantify the difference in redshift evolution; we find that the DCDM variations are still discrepant to the degree that we expect *Euclid* to be able to discriminate between them based on the shape of the redshift distribution of  $\text{SNR} > 5$  peaks. The mass loss in the DCDM becomes increasingly more apparent at low redshift. This is reflected in the DCDM signals as the suppression increases for  $z < 0.4$ , which can be interpreted as a larger fraction of low- $z$  lenses that lose enough mass to drop below the SNR threshold.

The comparison illustrates that the redshift evolution of WL peaks can constrain parts of the cosmological parameter space; as we have illustrated, it is sensitive to the neutrino mass. However, it also shows that changes in cosmology may result in degenerate signatures when using only WL peaks. For example, the most massive neutrinos run and LS8 are practically indistinguishable.

In Broxterman et al. (2024), we showed that even though the impact of cosmology on the number density of the WL peaks is greater than that of realistic baryonic feedback, the two signatures are degenerate. In this work, we have shown that changes in cosmology impact the redshift evolution of the number density of high-SNR WL peaks more than baryonic feedback is expected to do. Combining the redshift and WL convergence distributions can, therefore, not only help constrain cosmology, but also simultaneously calibrate baryonic feedback. The evolution of the redshift distribution of the WL peaks will yield the cosmology, while the number density of WL convergence peaks is sensitive to the baryonic feedback strength. However, as indicated by the Planck variation, not all cosmologies change the redshift distribution of the peaks. Baryonic feedback and changes in cosmology are thus still degenerate in certain parts of the parameter space. From the variations we explored, this seems to be the case for  $\Omega_m$  and baryonic feedback strength leading to lower gas fractions in low- $z$  clusters. However, more variations that jointly vary baryonic physics and cosmology should be compared in order to study this in more detail.

Ultimately, baryonic physics could be calibrated jointly while constraining cosmology by combining different WL statistics (see e.g. Semboloni et al. 2013), that are sensitive in different ways to cosmology and baryonic physics. This may be extended by including (the cross-correlation with) additional probes to inform on the strength of baryonic, such as SZ or X-ray (see e.g. McCarthy et al. 2023, 2024; Bigwood et al. 2024). In this section, we have argued that WL peaks will be useful in furthering this goal.

#### 4.5 Cosmology with the redshift of WL peaks

Next, we quantify the differences between the simulation variations to L1\_m9 to determine the feasibility of using WL peaks to constrain cosmology with Stage IV WL surveys. As we are interested in the shape of the distribution, as opposed to its amplitude, we use the Kolmogorov–Smirnov test. The non-parametric test evaluates the null hypothesis that two distributions are equal by comparing their cumulative density functions. For each of the L1 variations, we randomly draw the number of peaks corresponding to our *Euclid* DR3 estimate (i.e. corresponding to 14,000 deg<sup>2</sup> instead of the full light-cone) and compare this to the L1\_m9 distribution, which yields a  $p$ -value describing the hypothesis of the distributions being identi-

**Table 3.**  $p$ -value of the KS test of the null hypothesis that the shape of the number density as a function of WL convergence ( $p_\kappa$ ) or redshift ( $p_z$ ) of the  $\text{SNR} > 5$  WL peak distribution measured in a simulation variation is identical to L1\_m9. A high  $p$ -value indicates that the two distributions are statistically indistinguishable. Values with a  $p$ -value lower than 0.1 are indicated in bold. The shape of the WL convergence number densities differs between cosmology and baryonic variations. The shape of the redshift distribution depends primarily on cosmology and, to a much smaller degree, on baryonic feedback.

Identifier	$p_\kappa$	$p_z$
L1_m9_DMO	0.43	0.18
fgas+2 $\sigma$	0.38	0.16
fgas-2 $\sigma$	0.47	0.64
fgas-4 $\sigma$	0.16	0.67
fgas-8 $\sigma$	<b><math>7.9 \times 10^{-3}</math></b>	0.18
M*- $\sigma$	0.38	0.33
M*- $\sigma$ _fgas-4 $\sigma$	<b><math>1.8 \times 10^{-2}</math></b>	0.62
Jet	0.26	<b><math>6.6 \times 10^{-3}</math></b>
Jet_fgas-4 $\sigma$	<b><math>5.4 \times 10^{-3}</math></b>	0.45
Planck	<b><math>3.4 \times 10^{-2}</math></b>	0.56
PlanckNu0p24Var	<b><math>7.2 \times 10^{-3}</math></b>	$< 10^{-5}$
PlanckNu0p24Fix	$< 10^{-5}$	$< 10^{-5}$
PlanckNu0p48Fix	$< 10^{-5}$	$< 10^{-5}$
PlanckDCDM12	$< 10^{-5}$	<b><math>3.7 \times 10^{-2}</math></b>
PlanckDCDM24	$< 10^{-5}$	<b><math>1.2 \times 10^{-3}</math></b>
LS8	$< 10^{-5}$	$< 10^{-5}$

cal. We randomly draw a WL peak sample 1000 times and report the mean of the  $p$ -values for the WL convergence and redshift number densities in the second and third columns of Table 3, respectively. Entries with a greater value are more consistent with the fiducial simulation. In bold, we highlight all entries with a  $p$ -value lower than 0.1 to illustrate variations whose distribution differs most from L1\_m9. The differences in the  $\kappa$  distributions are generally greater than those in the redshift distributions. Similarly, the differences induced by the changes in cosmology are greater than those between the baryonic feedback variations.

Focusing first on the difference in the  $\kappa$  distributions, we expect all cosmology variations to result in number density distributions that are discrepant with L1\_m9 to the degree that should be measurable with the *Euclid* DR3 sample. At the same time, we see that some of the baryonic variations, specifically the simulations calibrated to  $fgas - 8\sigma$ ,  $M^* - \sigma$ \_fgas-4 $\sigma$  and Jet\_fgas-4 $\sigma$ , also result in similar differences. This means the baryonic feedback should be understood and modeled accurately before the  $\kappa$  number density of WL peaks can be exploited to constrain cosmology.

In contrast, based on the bold-valued entries for the  $p_z$ -values, we generally find that the baryonic feedback variations are consistent with L1\_m9, whereas the cosmology variations show great differences as all but Planck and the DCDM variations have  $p$ -values lower than  $10^{-5}$ . Only one baryonic feedback model, the Jet model, is found to have a redshift distribution with a shape statistically different from L1\_m9. This is not the case for the Jet model with stronger feedback, Jet\_fgas-4 $\sigma$ . The origin of this difference is unclear, but may indicate some dependence on the simulation’s AGN subgrid model.

If we carry out a similar test to compare  $fgas - 8\sigma$  to PlanckNu0p24Var we find that the corresponding  $p$ -values are  $p_\kappa = 0.48$  and  $p_z = 6.5 \times 10^{-5}$ , i.e. the shape of their distributions in WL convergence is indistinguishable while their redshift distributions are different. As these variations differ in terms of both

cosmology and baryonic feedback, the comparison highlights the degeneracy between cosmology and baryonic feedback in the the number density in WL convergence, which may be broken by including the redshift information.

To conclude, the  $p_z$  values confirm the result that the redshift distribution of WL peaks depends primarily on cosmology and, to a much smaller degree, on baryonic feedback strength. Therefore, the redshift distribution of high-valued SNR peaks provides an excellent probe to help constrain cosmology complementary to the commonly used peak height distribution.

## 5 SUMMARY AND CONCLUSIONS

In this paper, we have studied the cosmological potential of the redshift distribution of the expected measurement of high- $\kappa$  (SNR > 5) WL peaks for a Stage IV WL survey using the FLAMINGO cosmological hydrodynamical simulation suite. We measured the contribution to the WL convergence value along the line of sight for WL peaks that were selected from integrated maps, and we assigned the redshift of the most contributing overdensity to each peak. At the peak redshift, we match peaks to haloes to determine the origin of the WL peaks. We find that high-SNR peaks (SNR > 5) originate primarily from single massive haloes with  $M_{200c} > 10^{14} M_\odot$  (Fig. 2) and that more massive haloes preferentially cause higher- $\kappa$  peaks (Fig. 4). We estimate Stage IV WL surveys will detect  $5.5 \times 10^4$  ( $6.8 \times 10^3$ ) SNR > 5 (8) WL peaks with a purity, i.e. fraction belonging to a single massive halo along the line of sight, of 76 (96) per cent. For haloes with  $M_{200c} > 10^{14.5} M_\odot$ , we find a completeness, i.e. the percentage of haloes that is matched to a peak in our SNR > 5 peak sample, of 93 (59) per cent up to  $z = 0.5$  (1) (Fig. 5). The purity and completeness are competitive with state-of-the-art X-ray and SZ cluster abundance inferences. The paper has highlighted the possibility of using the WL peaks measured by upcoming Stage IV WL surveys. In the future, the distribution of the number density of WL peaks in WL convergence and redshift may be studied as a function of cosmology, as is done commonly for the HMF.

By matching each WL peak to individual haloes and by assigning a redshift, we have studied the impact of baryonic physics and cosmology on the redshift evolution of the number density of WL peaks. We have shown that, within the FLAMINGO simulation suite, the changes in baryonic feedback strength, as parameterized by the gas fraction in clusters and/or the  $z = 0$  galaxy stellar mass function, do not have a substantial impact on the redshift evolution of the sample of high-SNR WL peaks that will be measured by Stage IV WL surveys (Fig. 9). This includes models where the gas fractions in low- $z$  clustered are lowered by  $8\sigma$  compared to the fiducial model and a DMO+v simulation without baryons.

In contrast, changes in cosmology can have a strong impact on the redshift distribution of high-SNR WL peaks. From the variations we have explored, we find the redshift distribution is particularly sensitive to the neutrino mass, which impacts structure formation and the value of  $\sigma_8$ . However, more variations that jointly vary cosmology and baryonic physics should be carried out to further quantify which regions of cosmology and baryonic physics can be effectively constrained using the redshift distribution of WL peaks. Combining the redshift distribution of WL peaks with their number density as a function of the WL convergence can help simultaneously calibrate baryonic feedback and constrain cosmology, as the two statistics show different dependencies on baryonic physics. The constraining power can be increased by including other higher-order WL statistics

or by including (cross-correlations with) other observables, such as SZ or X-ray.

## ACKNOWLEDGEMENTS

RK acknowledges support by research programme Athena 184.034.002 from the Dutch Research Council (NWO). VJFM acknowledges support by NWO through the Dark Universe Science Collaboration (OCENW.XL21.XL21.025). This work used the DiRAC@Durham facility managed by the Institute for Computational Cosmology on behalf of the STFC DiRAC HPC Facility ([www.dirac.ac.uk](http://www.dirac.ac.uk)). The equipment was funded by BEIS capital funding via STFC capital grants ST/K00042X/1, ST/P002293/1, ST/R002371/1 and ST/S002502/1, Durham University and STFC operations grant ST/R000832/1. DiRAC is part of the National e-Infrastructure. We have relied on the numerical packages MATPLOTLIB (Hunter 2007), HEALPY (Zonca et al. 2019), NUMPY (Harris et al. 2020), SWIFTSIMIO (Borrow & Borisov 2020), and ASTROPY (Astropy Collaboration et al. 2022) for the analysis and plotting.

## DATA AVAILABILITY

The data supporting the figures in this article are available upon reasonable request to the corresponding author.

## REFERENCES

- Abbott T. M. C., et al., 2022, *Phys. Rev. D*, **105**, 023520
- Aihara H., et al., 2018, *PASJ*, **70**, S8
- Allen S. W., Evrard A. E., Mantz A. B., 2011, *ARA&A*, **49**, 409
- Amon A., et al., 2023, *MNRAS*, **518**, 477
- Aoyama S., Sekiguchi T., Ichiki K., Sugiyama N., 2014, *J. Cosmology Astropart. Phys.*, **2014**, 021
- Applegate D. E., et al., 2014, *MNRAS*, **439**, 48
- Asgari M., et al., 2021, *A&A*, **645**, A104
- Astropy Collaboration et al., 2022, *ApJ*, **935**, 167
- Aubourg É., et al., 2015, *Phys. Rev. D*, **92**, 123516
- Bartelmann M., Schneider P., 2001, *Phys. Rep.*, **340**, 291
- Benisty D., 2021, *Physics of the Dark Universe*, **31**, 100766
- Bernardeau F., van Waerbeke L., Mellier Y., 1997, *A&A*, **322**, 1
- Bigwood L., et al., 2024, *MNRAS*, **534**, 655
- Bilicki M., et al., 2021, *A&A*, **653**, A82
- Blas D., Lesgourgues J., Tram T., 2011, *J. Cosmology Astropart. Phys.*, **2011**, 034
- Bocquet S., Saro A., Dolag K., Mohr J. J., 2016, *MNRAS*, **456**, 2361
- Bocquet S., et al., 2023, *arXiv e-prints*, p. arXiv:2310.12213
- Bocquet S., et al., 2024, *arXiv e-prints*, p. arXiv:2401.02075
- Booth C. M., Schaye J., 2009, *MNRAS*, **398**, 53
- Borrow J., Borisov A., 2020, *Journal of Open Source Software*, **5**, 2430
- Borrow J., Schaller M., Bower R. G., Schaye J., 2022, *MNRAS*, **511**, 2367
- Broxterman J. C., et al., 2024, *MNRAS*, **529**, 2309
- Bulbul E., et al., 2024, *A&A*, **685**, A106
- Cacciato M., van den Bosch F. C., More S., Li R., Mo H. J., Yang X., 2009, *MNRAS*, **394**, 929
- Chaikin E., Schaye J., Schaller M., Benítez-Llambay A., Nobels F. S. J., Ploeckinger S., 2023, *MNRAS*, **523**, 3709
- Chen K.-F., et al., 2024, *arXiv e-prints*, p. arXiv:2406.11966
- Chiu I.-N., et al., 2024, *arXiv e-prints*, p. arXiv:2406.11970
- Chua K. T. E., Pillepich A., Vogelsberger M., Hernquist L., 2019, *MNRAS*, **484**, 476
- Coultoun W. R., Liu J., McCarthy I. G., Osato K., 2020, *MNRAS*, **495**, 2531
- Courtin J., Rasera Y., Alimi J. M., Corasaniti P. S., Boucher V., Füfze A., 2011, *MNRAS*, **410**, 1911

DESI Collaboration et al., 2024, [arXiv e-prints](#), p. arXiv:2404.03002

Dalla Vecchia C., Schaye J., 2008, [MNRAS](#), **387**, 1431

Dark Energy Survey and Kilo-Degree Survey Collaboration et al., 2023, [The Open Journal of Astrophysics](#), **6**, 36

Davies C. T., Cautun M., Giblin B., Li B., Harnois-Déraps J., Cai Y.-C., 2021, [MNRAS](#), **507**, 2267

Davies C. T., Cautun M., Giblin B., Li B., Harnois-Déraps J., Cai Y.-C., 2022, [MNRAS](#), **513**, 4729

Davies C. T., Harnois-Déraps J., Li B., Giblin B., Hernández-Aguayo C., Paillas E., 2024, [MNRAS](#), **533**, 3546

Debackere S. N. B., Hoekstra H., Schaye J., 2022, [MNRAS](#), **515**, 6023

Dietrich J. P., Hartlap J., 2010, [MNRAS](#), **402**, 1049

Elbers W., Frenk C. S., Jenkins A., Li B., Pascoli S., 2021, [MNRAS](#), **507**, 2614

Elbers W., et al., 2024, [arXiv e-prints](#), p. arXiv:2403.12967

Enqvist K., Nadathur S., Sekiguchi T., Takahashi T., 2015, [J. Cosmology Astropart. Phys.](#), **2015**, 067

Euclid Collaboration: Ajani V., Baldi M., Barthelemy A., et al., 2023, [A&A](#), **675**, A120

Euclid Collaboration: Blanchard A., Camera S., Carbone C., et al., 2020, [A&A](#), **642**, A191

Euclid Collaboration: Martinet N., Schrabback T., Hoekstra H., et al., 2019, [A&A](#), **627**, A59

Euclid Collaboration: Mellier Y., Abdurro'uf Acevedo Barroso J., et al., 2024, [A&A](#), accepted, p. arXiv:2405.13491

Euclid Collaboration: Pocino A., Tutusaus I., Castander F. J., et al., 2021, [A&A](#), **655**, A44

Fumagalli A., Costanzi M., Saro A., Castro T., Borgani S., 2024, [A&A](#), **682**, A148

Gatti M., et al., 2023, [Monthly Notices of the Royal Astronomical Society: Letters](#), **527**, L115

Ghirardini V., et al., 2024, [A&A](#), **689**, A298

Górski K. M., Hivon E., Banday A. J., Wandelt B. D., Hansen F. K., Reinecke M., Bartelmann M., 2005, [ApJ](#), **622**, 759

Grandón D., Marques G. A., Thiele L., Cheng S., Shirasaki M., Liu J., 2024, [arXiv e-prints](#), p. arXiv:2403.03807

Hamana T., Takada M., Yoshida N., 2004, [MNRAS](#), **350**, 893

Hamana T., Sakurai J., Koike M., Miller L., 2015, [PASJ](#), **67**, 34

Han J., Cole S., Frenk C. S., Benítez-Llambay A., Helly J., 2018, [MNRAS](#), **474**, 604

Harnois-Déraps J., et al., 2024, [arXiv e-prints](#), p. arXiv:2405.10312

Harris C. R., et al., 2020, [Nature](#), **585**, 357

Hilbert S., et al., 2020, [MNRAS](#), **493**, 305

Hildebrandt H., et al., 2017, [MNRAS](#), **465**, 1454

Hilton M., et al., 2021, [ApJS](#), **253**, 3

Hoekstra H., Jain B., 2008, [Annual Review of Nuclear and Particle Science](#), **58**, 99

Hunter J. D., 2007, [Computing in Science and Engineering](#), **9**, 90

Huško F., Lacey C. G., Schaye J., Schaller M., Nobels F. S. J., 2022, [MNRAS](#), **516**, 3750

Kacprzak T., et al., 2016, [MNRAS](#), **463**, 3653

Kaiser N., 1992, [ApJ](#), **388**, 272

Kaiser N., Squires G., 1993, [ApJ](#), **404**, 441

Kilbinger M., 2015, [Reports on Progress in Physics](#), **78**, 086901

Kratochvíl J. M., Haiman Z., May M., 2010, [Phys. Rev. D](#), **81**, 043519

Kugel R., et al., 2023, [MNRAS](#), **526**, 6103

Kugel R., Schaye J., Schaller M., McCarthy I. G., Braspennincx J., Helly J. C., Forouhar Moreno V. J., McGibbon R. J., 2024a, [arXiv e-prints](#), p. arXiv:2406.03180

Kugel R., Schaye J., Schaller M., Forouhar Moreno V. J., McGibbon R. J., 2024b, [arXiv e-prints](#), p. arXiv:2408.17217

Kuijken K., et al., 2019, [A&A](#), **625**, A2

LSST Science Collaboration et al., 2009, [arXiv e-prints](#), p. arXiv:0912.0201

Lesgourgues J., Pastor S., 2006, [Phys. Rep.](#), **429**, 307

Li Z., Liu J., Zorrilla Matilla J. M., Coulton W. R., 2019, [Phys. Rev. D](#), **99**, 063527

Li Z., Liu X., Fan Z., 2023, [MNRAS](#), **520**, 6382

Limber D. N., 1953, [ApJ](#), **117**, 134

Liu J., Haiman Z., 2016, [Phys. Rev. D](#), **94**, 043533

Liu J., Petri A., Haiman Z., Hui L., Kratochvíl J. M., May M., 2015, [Phys. Rev. D](#), **91**, 063507

LoVerde M., Afshordi N., 2008, [Phys. Rev. D](#), **78**, 123506

Lu T., Haiman Z., 2021, [MNRAS](#), **506**, 3406

Manz A., Giannantonio T., Weller J., Hoyle B., Hütsi G., Sartoris B., 2013, [MNRAS](#), **434**, 684

Martinet N., et al., 2018, [MNRAS](#), **474**, 712

Martizzi D., Mohammed I., Teyssier R., Moore B., 2014, [MNRAS](#), **440**, 2290

McCarthy I. G., Le Brun A. M. C., Schaye J., Holder G. P., 2014, [MNRAS](#), **440**, 3645

McCarthy I. G., Bird S., Schaye J., Harnois-Déraps J., Font A. S., van Waerbeke L., 2018, [MNRAS](#), **476**, 2999

McCarthy I. G., et al., 2023, [MNRAS](#),

McCarthy I. G., et al., 2024, [arXiv e-prints](#), p. arXiv:2410.19905

Medezinski E., et al., 2018, [PASJ](#), **70**, S28

Nagai D., Vikhlinin A., Kravtsov A. V., 2007, [ApJ](#), **655**, 98

Oguri M., Miyazaki S., 2024, [arXiv e-prints](#), p. arXiv:2409.12361

Oguri M., et al., 2018, [PASJ](#), **70**, S20

Philcox O. H. E., Ivanov M. M., 2022, [Phys. Rev. D](#), **105**, 043517

Planck Collaboration et al., 2020a, [A&A](#), **641**, A6

Planck Collaboration et al., 2020b, [A&A](#), **641**, A8

Ploeckinger S., Schaye J., 2020, [MNRAS](#), **497**, 4857

Reid B., et al., 2016, [MNRAS](#), **455**, 1553

Reiprich T. H., Böhringer H., 2002, [ApJ](#), **567**, 716

Riess A. G., Casertano S., Yuan W., Bowers J. B., Macri L., Zinn J. C., Scolnic D., 2021, [ApJ](#), **908**, L6

Rykoff E. S., et al., 2014, [ApJ](#), **785**, 104

Schaller M., et al., 2024, [MNRAS](#), **530**, 2378

Schaye J., Dalla Vecchia C., 2008, [MNRAS](#), **383**, 1210

Schaye J., et al., 2023, [MNRAS](#), **526**, 4978

Scoccimarro R., 2004, [Phys. Rev. D](#), **70**, 083007

Secco L. F., et al., 2022, [Phys. Rev. D](#), **105**, 023515

Semboloni E., Hoekstra H., Schaye J., 2013, [MNRAS](#), **434**, 148

Shan H., et al., 2018, [MNRAS](#), **474**, 1116

Spergel D., et al., 2015, [arXiv e-prints](#), p. arXiv:1503.03757

Stanek R., Rudd D., Evrard A. E., 2009, [MNRAS](#), **394**, L11

Takahashi R., Nishimichi T., Namikawa T., Taruya A., Kayo I., Osato K., Kobayashi Y., Shirasaki M., 2020, [ApJ](#), **895**, 113

Tröster T., et al., 2020, [A&A](#), **633**, L10

Upadhye A., et al., 2023, [arXiv e-prints](#), p. arXiv:2308.09755

Vakili M., et al., 2023, [A&A](#), **675**, A202

Velliscig M., van Daalen M. P., Schaye J., McCarthy I. G., Cacciato M., Le Brun A. M. C., Dalla Vecchia C., 2014, [MNRAS](#), **442**, 2641

Velliscig M., et al., 2015, [MNRAS](#), **453**, 721

Wang L., Steinhardt P. J., 1998, [ApJ](#), **508**, 483

Weiss A. J., Schneider A., Sgier R., Kacprzak T., Amara A., Refregier A., 2019, [J. Cosmology Astropart. Phys.](#), **2019**, 011

Wen Z. L., Han J. L., 2015, [ApJ](#), **807**, 178

Wiersma R. P. C., Schaye J., Theuns T., Dalla Vecchia C., Tornatore L., 2009, [MNRAS](#), **399**, 574

Xhakaj E., Leauthaud A., Lange J., Krause E., Hearin A., Huang S., Wechsler R. H., Heydenreich S., 2024, [MNRAS](#), **530**, 4203

Yang X., Kratochvíl J. M., Wang S., Lim E. A., Haiman Z., May M., 2011, [Phys. Rev. D](#), **84**, 043529

Zonca A., Singer L., Lenz D., Reinecke M., Rosset C., Hivon E., Gorski K., 2019, [Journal of Open Source Software](#), **4**, 1298

van Waerbeke L., 2000, [MNRAS](#), **313**, 524

## APPENDIX A: SMOOTHING

In this Appendix, we study the impact of the adopted smoothing scale on the halo peak matching. The fiducial smoothing scale adopted in this work is 1 arcmin. In Fig. A1, we show the results of the completeness of the halo peak matching for three additional smoothing scales: 0.5' (upper left), 1' (upper right), 3' (lower left), and 10' (lower

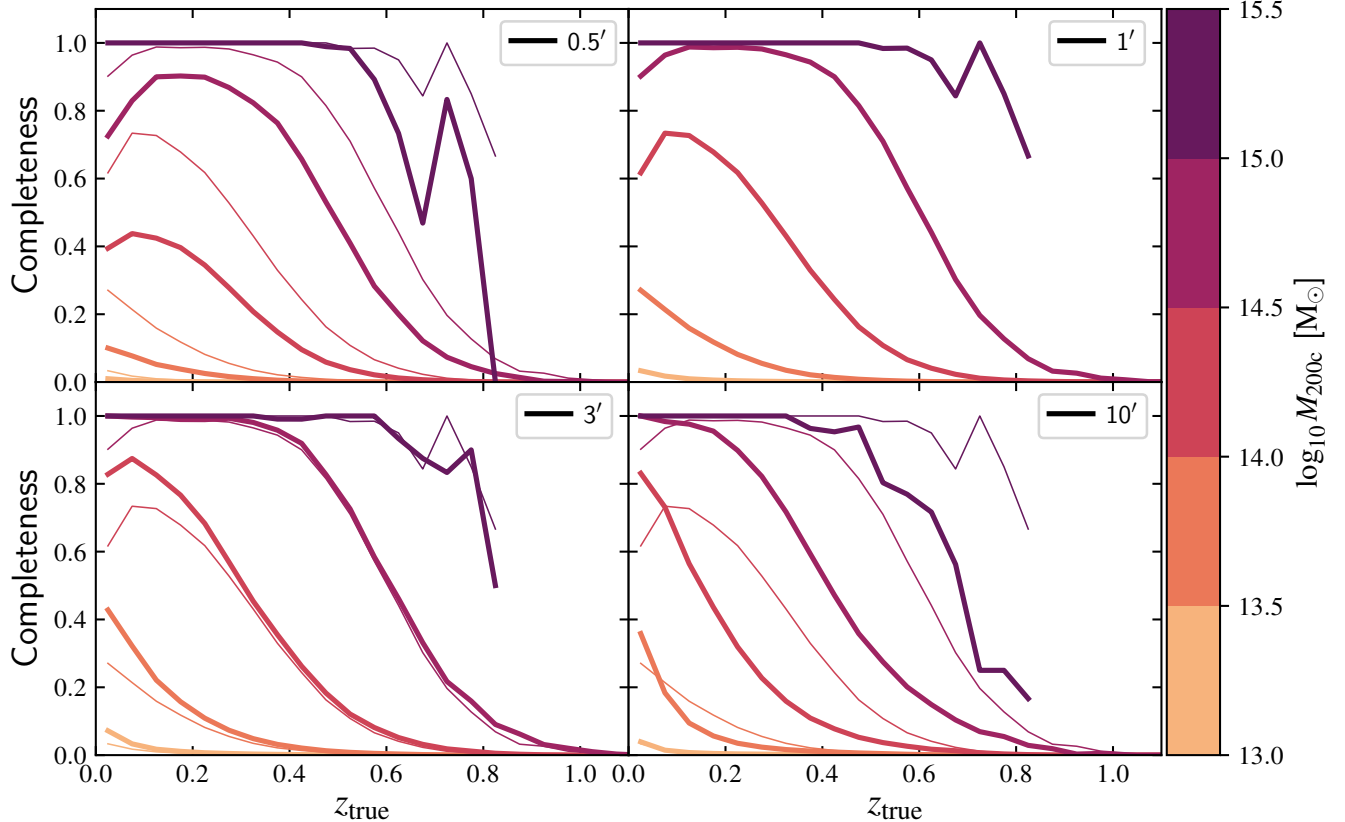


**Figure A1.** Completeness, i.e. the fraction of haloes within a halo mass bin matched to an  $\text{SNR} > 5$  WL peak for the four different smoothing scales, as indicated in the upper right of each panel. The results for 1 arcmin smoothing are repeated in all panels as thin curves. For small smoothing scales, some massive haloes at low redshift that span an angular size larger than is smoothed over will be missed as the smoothing scale is too small to achieve the optimal SNR. At the same time, increasing the smoothing scale will result in lower completeness at high redshift as those objects subtend smaller sizes, and increasing the smoothing will decrease the SNR of those objects. Combining smoothing scales may thus improve the amount of information that is extracted.

right). The curves corresponding to  $1'$  smoothing are repeated as thin lines in each panel.

For each smoothing scale, the figure shows the completeness, i.e. the fraction of haloes matched to a peak (with  $\text{SNR} > 5$ ) within a halo mass bin. As already mentioned in Section 4.2, the small drop in completeness at low redshift for the  $M_{200c} = 10^{14} - 10^{15} \text{ M}_\odot$  mass bins is the result of the smoothing scale being too small to achieve the optimal SNR for these objects. At  $z = 0.1$ , the smoothing scale of  $1'$  corresponds to a physical scale of  $\approx 110 \text{ kpc}$ , which is an order of magnitude smaller than the viral radius of  $M_{200c} \geq 10^{14} \text{ M}_\odot$  haloes.

This smoothing scale is, therefore, too small to achieve the optimal SNR for these haloes. This is illustrated by the fact that the completeness of the same halo mass bins is larger when  $3'$  smoothing has been applied. The most massive haloes ( $M_{200c} \geq 10^{15} \text{ M}_\odot$ ) do not suffer from this problem, as they are so massive that independent of the smoothing scale, they will cause a large enough WL peak to be detected. A larger smoothing scale than the fiducial  $1'$  will allow the detection of more low- $z$  objects as this scale corresponds better to the angular size of the objects we are probing. However, simultaneously, the completeness at higher  $z$  drops for larger smoothing scales as the objects have a smaller angular scale at higher redshifts.

Ideally, the smoothing scale should be matched to the redshift of an object such that an appropriate scale can be chosen that smooths over the entire object but not over a larger area than necessary, as

having either a too-small or too-large smoothing scale will decrease the SNR of the object. As the redshift of an object is not known beforehand, it is not clear what the optimal smoothing scale is to detect an object until it has already been detected and identified with an optical counterpart, and the choice of smoothing scale is a trade-off between detecting more objects at higher redshift against lower completeness at lower redshift. We chose a  $1'$  smoothing scale as the fiducial scale to keep the results consistent with Broxterman et al. (2024). However, we already noted that multiple smoothing scales may be combined to probe information from different scales.

## APPENDIX B: NOISE PEAK DISTRIBUTION

In this Appendix, we compare the number density of WL peaks for our *Euclid*-like sample to a distribution generated only by noise. The noise field is generated as described in Section 3.2. In the regular procedure, we add the noise to the WL convergence field and then smooth the map. The number density of WL peaks selected from this map is indicated by the solid curve in Fig. B1. Now, we also show the peak distribution that is obtained if we directly determine the peaks from the smoothed noise map ('Smoothed noise peaks'), which do not contain any cosmological information. The Smoothed noise peak distribution is indicated by the dashed curve. Whereas the noise is a normal distribution centred on  $\kappa = 0$ , the Smoothed noise

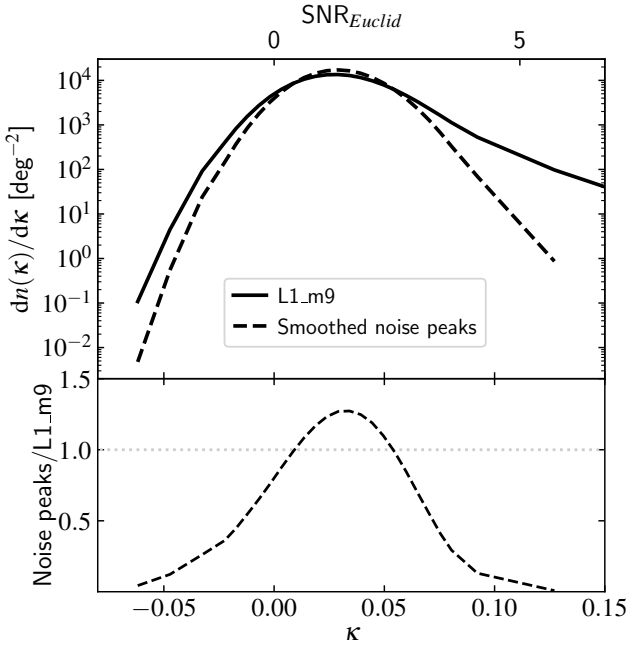


**Figure B1.** Top: number density of WL peaks for the WL convergence map that includes noise and smoothing (solid curve) and of only the smoothed noise (dashed curve). Bottom: ratio of the smoothed noise peak distribution to L1\_m9. The smoothed noise peak distribution dominates the signal for  $0 \lesssim \kappa \lesssim 0.07$ , and lower and higher valued peaks generally correspond to physical objects.

peak distribution, consisting of the local maxima of the smoothed noise map, has a positive mean and an asymmetric shape.

In Fig. 2, we illustrated that the Noise peak distribution peaks at  $\kappa \approx 0.04$ . Fig. B1 illustrates that this is also the WL convergence value at which the distribution from the applied noise field peaks. As expected, for larger  $\kappa$  values, the distribution of Smoothed noise peak decreases, and the majority of the L1\_m9 peaks are no longer caused by the noise, as also already shown in Fig. 2. Similarly, the lowest valued WL peaks, with  $\kappa \lesssim 0$ , are also increasingly less likely to be caused by the random noise. These peaks, therefore, correspond to the local maxima in void regions in the simulations.

## APPENDIX C: HALO-PEAK MATCHING CHARACTERISTICS

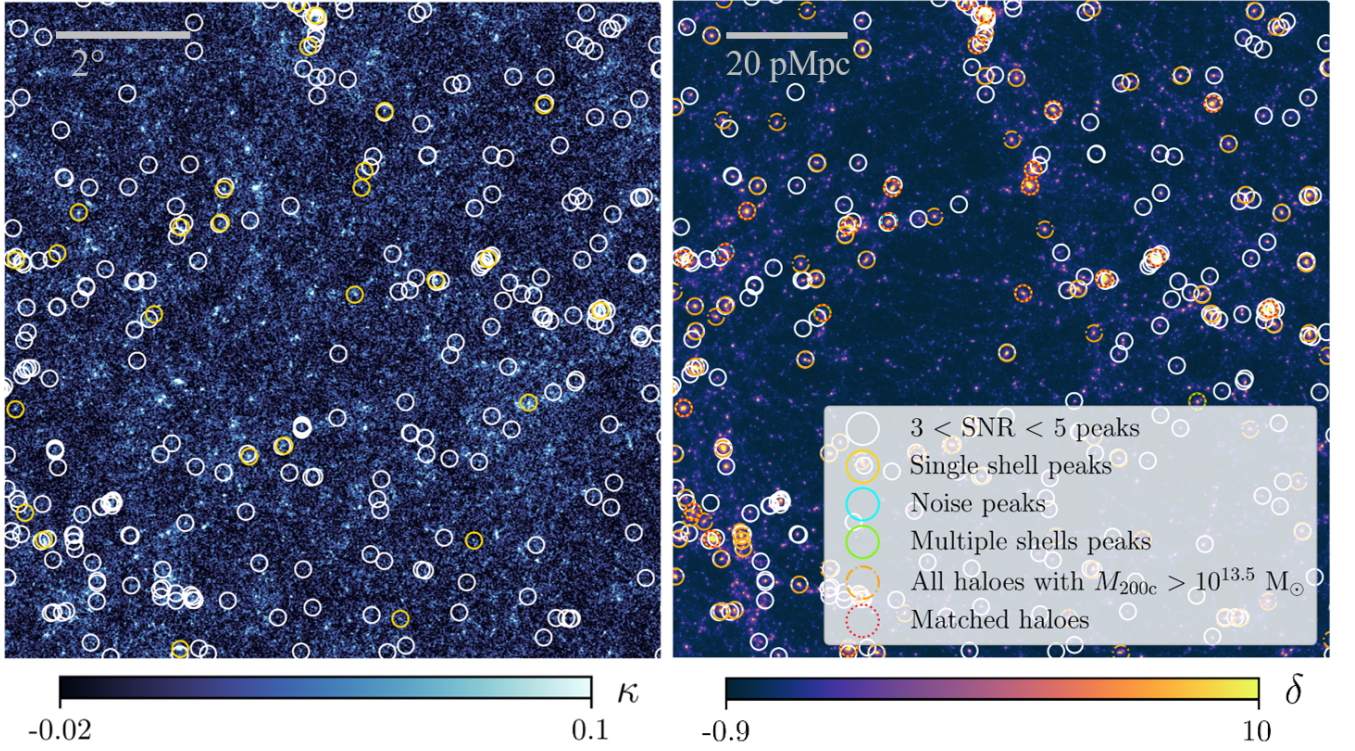
In this Appendix, we study the characteristics of the peak-halo matching algorithm in more detail. In Fig. C1, we show the same fields as in Fig. 3, but we split the peaks into the three peak categories we considered in this work. The solid yellow, cyan, and green circles indicate the Single shell, Noise, and Multiple shells peaks, respectively. We also show all  $M_{200c} > 10^{13.5} M_\odot$  haloes from the FLAMINGO halo light-cone as dashed-dotted white circles and the matched haloes as dotted red circles.

Fig. C1 shows that Noise and Multiple shells peaks may still correspond to massive overdense objects. For example, a Noise peak is indicated by the solid cyan circle in the middle left of the figure. Similarly, the solid green circle directly above the legend shows that this Multiple shells peak can also be assigned to a halo at the same angular position. When comparing the redshift distribution of the peaks, we have also assigned a redshift to the Noise peaks and

Multiple shells peaks. In any observational inference, we will not know which peaks are Noise peaks or Multiple shells peaks, but can only assign a redshift based on the galaxies at the position of the peak. The comparison here shows that this is a valid approach, as there are still haloes assigned that contribute significantly.

In orange, we show the WL peaks assigned to this shell with an SNR of 3 – 5. These are lower values than the standard range we consider in this work. The figure shows that most of these peaks still clearly correspond to an overdense structure in the field, as indicated by the white dashed-dotted circles. Lowering the SNR threshold would allow us to include these matches in samples we consider and possibly get tighter constraints, but this comes at the cost of decreasing the purity of the sample, as shown in Fig. 2. As a result, the interpretation will be more difficult, as a superposition of objects or noise will cause more WL peaks, and interpreting them each as arising from a single halo along the line of sight will no longer be justified. This is also clear from the fact that some of these peaks do not correspond to a massive overdense structure. However, we stress that our chosen SNR cut-off may not be optimal. Additional work should be done to explore the optimal SNR cut-off value to balance the trade-off between cosmological information and purity.

This paper has been typeset from a  $\text{\TeX}/\text{\LaTeX}$  file prepared by the author.



**Figure C1.** Same as Fig. 3 and now also showing the different peak categories to which the peaks belong. The Single shell peaks (solid yellow), Noise peaks (solid cyan), Multiple shells peaks (solid green), peaks assigned to this shell with  $\text{SNR} = 3 - 5$  (solid white), all  $\log_{10} M_{200c} [\text{M}_\odot] > 13.5$  haloes (dashed-dotted orange) and haloes that have been matched to an  $\text{SNR} > 5$  peak (dotted red). Most Noise and Multiple shells peaks are still visibly well matched to a halo at their position. The apparent overdensities that do not generate an  $\text{SNR} > 5$  peak produce peaks with an  $\text{SNR}$  value lower than this cut.